

Comparing 1-year GUMICS–4 simulations of the Terrestrial Magnetosphere with Cluster Measurements

G. Facskó^{1,2,3}, D. G. Sibeck², I. Honkonen⁴, J. Bór⁵, G. Farinas Perez^{2,3*},
A. Timár¹, Y. Y. Shprits^{6,7}, P. Peitso^{8†}, L. Degener^{4‡}, E. I. Tanskanen^{8,9},
C. R. Anekallu¹⁰, J. Kalmár⁵, S. Szalai^{5,11}, Á. Kis⁵, V. Wesztergom⁵

¹Wigner Research Centre for Physics, Budapest, Hungary

²NASA Goddard Space Flight Center, Greenbelt, Maryland, USA

³the Catholic University of America, Washington DC, USA

⁴Finnish Meteorological Institute, Helsinki, Finland

⁵Institute of Earth Physics and Space Science (ELKH EPSS), Sopron, Hungary

⁶Helmholtz Centre Potsdam, GFZ German Research Centre for Geosciences, Potsdam, Germany

⁷Institute for Physics and Astronomy, University of Potsdam, Potsdam, Germany

⁸Sodankylä Geophysical Observatory, University of Oulu, Sodankylä, Finland

⁹Department of Electronics and Nanoengineering, Aalto University, Espoo, Finland

¹⁰UCL Department of Space & Climate Physics, Mullard Space Science Laboratory, Dorking, UK

¹¹University of Miskolc, Department of Geophysics, Miskolc, Hungary

Key Points:

- The GUMICS–4 code provides realistic ion plasma moments and magnetic field in the solar wind and the outer magnetosheath.
- The code predicts realistic bow shock locations.
- An inner magnetosphere model should be added to the code to increase the accuracy of the simulation in the inner magnetosphere.

*Now at University of Miami, Electrical and Computer Engineering Department, Miami, Florida, USA

†Now at Aurora Propulsion Technologies, Espoo, Finland

‡Now private individual, Hannover, Germany

Corresponding author: Gábor Facskó, facsko.gabor@wigner.hu

23 **Abstract**

24 We compare the predictions of the GUMICS–4 global magnetohydrodynamic model for
 25 the interaction of the solar wind with the Earth’s magnetosphere with Cluster SC3 mea-
 26 surements for over one year, from January 29, 2002, to February 2, 2003. In particular,
 27 we compare model predictions with the north/south component of the magnetic field (B_z)
 28 seen by the magnetometer, the component of the velocity along the Sun-Earth line (V_x),
 29 and the plasma density as determined from a top hat plasma spectrometer and the space-
 30 craft’s potential from the electric field instrument. We select intervals in the solar wind,
 31 the magnetosheath, and the magnetosphere where these instruments provided good qual-
 32 ity data and the model correctly predicted the region in which the spacecraft is located.
 33 We determine the location of the bow shock, the magnetopause and, the neutral sheet
 34 from the spacecraft measurements and compare these locations to those predicted by the
 35 simulation.

36 The GUMICS–4 model agrees well with the measurements in the solar wind how-
 37 ever its accuracy is worse in the magnetosheath. The simulation results are not realis-
 38 tic in the magnetosphere. The bow shock location is predicted well, however, the mag-
 39 netopause location is less accurate. The neutral sheet positions are located quite accu-
 40 rately thanks to the special solar wind conditions when the B_y component of the inter-
 41 planetary magnetic field is small.

42 **1 Introduction**

43 One of the most cost-effective ways to study the interaction of the solar wind with
 44 planetary magnetospheres (or predict conditions in near-Earth space) is modeling this
 45 complex system using a magnetohydrodynamic (MHD) code. In the past, several par-
 46 allelized codes were developed, which are used for forecasting the near-Earth space en-
 47 vironment. Such as the Lyon-Fedder-Mobarry [LFM; *Lyon et al.*, 2004] code, the Grid
 48 Agnostic MHD for Extended Research Applications [GAMERA; *Zhang et al.*, 2019], the
 49 Open Geospace General Circulation Model [OpenGGCM; *Raeder et al.*, 2008], or the Block-
 50 Adaptive-Tree-Solarwind-Roe-Upwind-Scheme [BATS-R-US; *Powell et al.*, 1999; *Tóth
 et al.*, 2012]. In Europe three global MHD codes have been developed: the Grand Uni-
 52 fied Magnetosphere–Ionosphere Coupling Simulation [GUMICS–4; *Janhunen et al.*, 2012],
 53 the Computational Object–Oriented Libraries for Fluid Dynamics [COOLFluiD; *Lani
 et al.*, 2012] and the 3D resistive magnetohydrodynamic code Gorgon [*Chittenden et al.*,

55 2004; *Ciardi et al.*, 2007]. The COOLFluiD is a general-purpose plasma simulation tool.
 56 The Gorgon code was developed to study high-energy, collisional plasma interactions
 57 and has been adapted to simulate planetary magnetospheres and their interaction with
 58 the solar wind [*Mejnertsen et al.*, 2016, 2018]. Neither Gorgon nor COOLfluid has an
 59 ionospheric solver. Almost all of these codes are available at the Community Coordinated
 60 Modelling Center (CCMC; <http://ccmc.gsfc.nasa.gov/>) hosted by the NASA Goddard
 61 Space Flight Center (GSFC) or the Virtual Space Weather Modelling Centre (VSWMC;
 62 <http://swe.ssa.esa.int/web/guest/kul-cmpa-federated>; requires registration for the Eu-
 63 ropean Space Agency (ESA) Space Situational Awareness (SSA) Space Weather (SWE)
 64 portal) hosted by the KU Leuven [*Poedts et al.*, 2020]. A comparison of the simulation
 65 results with spacecraft and ground-based measurements is necessary to understand the
 66 abilities and features of the developed tools. A statistical study using long-term global
 67 MHD runs for validation of the codes seems necessary. Because providing long simula-
 68 tions is costly and time-consuming, only a few studies have been done, almost all for pe-
 69 riods much less than a year except *Liemohn et al.* [2018].

70 *Guild et al.* [2008a,b] launched two months of LFM runs and compared the plasma
 71 sheet properties in the simulated tail with the statistical properties of six years of Geo-
 72 tail magnetic field and plasma observations [*Kokubun et al.*, 1994; *Mukai et al.*, 1994].
 73 The LFM successfully reproduced the global features of the global plasma sheet in a sta-
 74 tistical sense. However, there were some differences. The predicted plasma sheet was too
 75 cold, too dense, and the bulk flow was faster than the observed plasma sheet [*Kokubun*
 76 *et al.*, 1994; *Mukai et al.*, 1994]. The LFM overestimated the ionospheric transpolar po-
 77 tential. The transpolar potential correlated with the speed of the plasma sheet flows. Equa-
 78 torial maps of density, thermal pressure, thermal energy and, velocity were compared.
 79 The LFM overestimated the plasma sheet density close to the Earth, the temperature
 80 by a factor of ~ 3 and the global average flow speed by a factor of ~ 2 . The LFM repro-
 81 duced many of the climatological features of the Geotail data set. The low-resolution model
 82 underestimated the occurrence of the fast earthward and tailward flows. Increasing the
 83 simulation resolution resulted in the development of fast, bursty flows. These flows in-
 84 fluenced the statistics and contributed to a better agreement between simulations and
 85 observations.

86 *Zhang et al.* [2011] studied the statistics of magnetosphere-ionosphere (MI) cou-
 87 pling using the LFM simulation of *Guild et al.* [2008a] above. The polar cap potential

and the field-aligned currents (FAC), the downward Poynting flux and, the vorticity of the ionospheric convection were compared with observed statistical averages and the Weimer05 empirical model [Weimer, 2005]. The comparisons showed that the LFM model produced quite accurate average distributions of the Region 1 (R1) and Region 2 (R2) currents. The ionospheric R2 currents in the MHD simulation seemed to originate from the diamagnetic ring current. The average LFM R1 and R2 currents were small compared with the values from the Weimer05 model. The average Cross Polar Cap Potential (CPCP) was higher in the LFM simulation than the measurements of the SuperDARN and the Weimer05 model. The average convention pattern was quite symmetric in the LFM simulation as compared to the SuperDARN measurements and the Weimer05 model. The SuperDARN measurements and the Weimer05 model had a dawn-dusk asymmetry. In the LFM model, more Poynting flux flowed into the polar region ionosphere than in the Weimer05 model as a consequence of the larger CPCP in the LFM simulation. The larger CPCP allowed a higher electric field in the polar region. The statistical dependence of the high-latitude convection patterns on Interplanetary Magnetic Field (IMF) clock angle was similar to the SuperDARN measurements [Sofko *et al.*, 1995] and the Weimer05 model. The average ionospheric field-aligned vorticity showed good agreement on the day-side. However, the LFM model gave larger nightside vorticity than SuperDARN measurements because the Pedersen conductance on the night side ionosphere was too low.

Wiltberger et al. [2017] studied the structure of high latitude field-aligned current patterns using three resolutions of the LFM global MHD code and the Weimer05 empirical model [Weimer, 2005]. The studied period was a month-long and contained two high-speed streams. Generally, the patterns agreed well with results obtained from the Weimer05 computing. As the resolution of the simulations increased, the currents became more intense and narrow. The ratio of the Region 1 (R1), the Region 2 (R2) currents and, the R1/R2 ratio increased when the simulation resolution increases. However, both the R1 and R2 currents were smaller than the predictions of the Weimer05 model. This effect led to a better agreement of the LFM simulation results with the Weimer 2005 model results. The CPCP pattern became concentrated in higher latitudes because of the stronger R2 currents. The relationship of the CPCP and the R1 looked evident at a higher resolution of the simulation. The LFM simulation could have reproduced the statistical features of the field-aligned current (FAC) patterns.

120 *Hajducek et al.* [2017] simulated the month of January 2005 using the Space Weather
 121 Modelling Framework [SWMF; *Tóth et al.*, 2005] and the OMNI solar wind data (<https://omniweb.gsfc.nasa.gov/>)
 122 as input. The simulations were executed with and without an inner magnetosphere model
 123 and using two different grid resolutions in the magnetosphere. The model was very good
 124 in predicting the ring currents [SYM-H; <http://wdc.kugi.kyoto-u.ac.jp/aeasy/asy.pdf>;
 125 *Iyemori*, 1990]. The K_p index (a measure of the general magnetospheric convention and
 126 the auroral currents [*Bartels et al.*, 1939; *Rostoker*, 1972; *Thomsen*, 2004]) was predicted
 127 well during storms however the index was overestimated during quiet periods. The AL
 128 index (that describes the westward electrojet of the surface magnetic field introduced
 129 by *Davis and Sugiura* [1966]) was predicted reasonably well on average. However, the
 130 model reached the highest negative AL value less often than it was reached in observa-
 131 tions because the model captured the structure of the auroral zone currents poorly. The
 132 overpredicting of K_p index during quiet times might have happened for the same rea-
 133 son because it is also sensitive to auroral zone dynamics. The SWMF usually over-predicted
 134 the CPCP. These results were not sensitive to grid resolutions, except for of the AL in-
 135 dex, which reached the highest negative value more often when the grid resolution was
 136 higher. Switching the inner magnetosphere model off had a negative effect on the accu-
 137 racy of all quantities mentioned above, except the CPCP.

138 This paper compares the Cluster SC3 measurements directly to a previously made
 139 1-year long GUMICS-4 simulation at locations in the solar wind, magnetosheath, and
 140 the magnetosphere along the Cluster SC3 orbit [...] [*Facskó et al.*, 2016]. The param-
 141 eters are B_z , the north/south component of the magnetic field in GSE coordinates, the
 142 solar wind velocity GSE X component (V_x), and the solar wind density n . We also com-
 143 pare the predicted and observed locations of the bow shock, magnetopause, and the neu-
 144 tral sheet. These parameters are selected because B_z controls the solar wind-magnetosphere
 145 interaction, V_x is the main component of the solar wind velocity and n is the ion plasma
 146 moment that is the easiest to calculate; furthermore, several instruments could deter-
 147 mine it (see Section 2.2). The structure of this paper is as follows. Section 2 describes
 148 the GUMICS-4 code, the 1-year simulation, and the Cluster spacecraft measurements.
 149 Section 3 gives comparisons between the simulations and observations. Results of the
 150 comparison are discussed in Section 4. Finally, Section 5 contains the conclusions.

151 **2 The GUMICS–4 products and Cluster measurements**

152 Here we use two very different time series. The first type is derived from a previ-
 153 ous 1-year run of the GUMICS–4 simulation [Facskó *et al.*, 2016]. The second time se-
 154 ries was measured by the magnetometer, ion plasma, and electric field instruments of
 155 the Cluster reference spacecraft.

156 **2.1 The GUMICS–4 code**

157 The GUMICS–4 model has two coupled simulation domains, the magnetospheric
 158 domain outside of a $3.7 R_E$ radius sphere around the Earth, and a coupled ionosphere
 159 module containing a 2D height-integrated model of ionosphere. GUMICS–4 is not a par-
 160 allel code model however it has been extensively used to study energy propagation from
 161 the solar wind into the magnetosphere through the magnetopause and other features [Jan-
 162 hunen *et al.*, 2012, see the references therein]. The code has also been applied to study
 163 forced reconnection in the tail [Vörös *et al.*, 2014]. Recently, several hundred synthetic
 164 two hours duration GUMICS–4 simulation runs were made to compare the simulation
 165 results to empirical formulas [Gordeev *et al.*, 2013]. The agreement was quite good in
 166 general, but the diameter of the magnetopause in the simulations deviated slightly (10 %)
 167 from corresponding observations in the tail. The GUMICS–4 simulation magnetotail was
 168 smaller than that which the spacecraft observed. However, the modeled magnetopause
 169 showed good agreement with the empirical model in the mid-tail at northward IMF con-
 170 ditions. Facskó *et al.* [2016] made a 1-year long simulation using the GUMICS–4 code.
 171 In those simulations, the magnetotail was significantly shorter than that which the space-
 172 craft observed [Facskó *et al.*, 2016]. Gordeev *et al.* [2013] and Vörös *et al.* [2014] had sim-
 173 ilar experience when the simulations of the papers were evaluated. Juusola *et al.* [2014]
 174 compared the ionospheric currents, fields and the Cross Polar Cap Potential Drop (CPCP)
 175 in the simulation to observations from the Super Dual Auroral Radar Network (Super-
 176 DARN) radars [Greenwald *et al.*, 1995] and CHAMP spacecraft [Reigber *et al.*, 2002] ob-
 177 servations of field-aligned currents (FAC) [Juusola *et al.*, 2007; Ritter *et al.*, 2004]. The
 178 CPCP, the FAC, and other currents could not be reproduced properly. A possible cause
 179 for this poor agreement could be the model's low resolution in the inner magnetosphere
 180 and/or the lack of an inner magnetosphere model accurately incorporating the physics
 181 of this region. This hypothesis is supported by the result of Haiducek *et al.* [2017]. Haiducek
 182 *et al.* [2017] simulated only a month-long period using a different spatial resolution and

183 tested the code with the inner magnetosphere model of the SWMF switched off for a spe-
 184 cial run. This run without an inner magnetosphere model made it clear that only the
 185 CPCP parameter of the simulation agreed quite well with the measurements. This fact
 186 explained why the agreement between the Cluster SC3 and the GUMICS-4 simulations
 187 was so good as described by *Lakka et al.* [2018a,b] based on the CPCP in GUMICS-4
 188 simulations. *Kallio and Facskó* [2015] determined plasma and magnetic field parame-
 189 ters along the lunar orbit from *Facskó et al.* [2016]'s global MHD simulations. The pa-
 190 rameters differed significantly from observations in the magnetotail indicating the need
 191 for future studies. *Facskó et al.* [2016] determined the footprint of Cluster SC3 using the
 192 1-year simulation and the Tsyganenko T96 empirical model [*Tsyganenko*, 1995]. The agree-
 193 ment of the footprint was better in the Northern Hemisphere. The GUMICS-4 tail was
 194 shorter in the simulations than the observations.

195 A 1-year global MHD simulation was produced with the GUMICS-4 code using
 196 the OMNI solar wind data from January 29, 2002, to February 2, 2003, as input [*Facskó*
 197 *et al.*, 2016]. The creation and analysis of the simulation were based on a work package
 198 of the European Cluster Assimilation Technology (ECLAT) project (https://cordis.europa.eu/result/rcn/165813_en.html)
 199 <http://www.eclat-project.eu/>). The GUMICS-4 is a serial code [*Janhunen et al.*, 2012]
 200 hence the 1-year simulation was made in 1860 independent runs. This interval covered
 201 155 Cluster SC3 orbits and each orbit lasted 57 hours. The FMI supercomputer at the
 202 time had 12 cores on each node hence the 57 hours were divided into 4.7 hours simula-
 203 tion time with one hour initialization period. Each sub-interval used its own individual
 204 average Geocentric Solar Ecliptic (GSE) IMF magnetic field X component B_x com-
 205 ponent and dipole tilt angle. All data gaps in the solar wind were interpolated linearly. If
 206 the data gap of the input file was at the beginning (or the end) of the interval then the
 207 first (or last) good data from the input file was used to fill the gap. The initialization
 208 of each simulation run was made using constant values. These values were the first valid
 209 data of the input file repeated 60 times (60 minutes) in the input file of the sub-interval.
 210 The simulation results were saved every five minutes. Various simulation parameters, for
 211 example, the density, particle density, temperature, magnetic field, solar wind velocity
 212 (29 different quantities) were saved from the simulation results along the Cluster refer-
 213 ence spacecraft's orbit in the GSE coordinates.

214 **2.2 The Cluster SC3 measurements**

215 The Cluster-II mission of the European Space Agency (ESA) was launched in 2000
 216 to observe geospace [Credland *et al.*, 1997; Escoubet *et al.*, 2001]. The four spacecraft form
 217 a tetrahedron in space however here we use only the measurements of the reference space-
 218 craft, Cluster SC3. The spacecraft was spin-stabilized and its rotation period is \sim 4 s.
 219 Hence, the intrinsic time resolution of the plasma instruments is 4 s and we use 4 s av-
 220 eraged magnetic field data. The highest resolution of the Cluster FluxGate Magnetome-
 221 ter (FGM) magnetic field instrument is 27 Hz [Balogh *et al.*, 1997, 2001]. The ion plasma
 222 data are provided by the Cluster Ion Spectrometry (CIS) Hot Ion Analyser (HIA) sub-
 223 instrument [Reme *et al.*, 1997; Rème *et al.*, 2001]. The CIS HIA instrument is calibrated
 224 using the Waves of HIgh frequency Sounder for Probing the Electron density by Relax-
 225 ation (WHISPER) wave instrument onboard Cluster [Décréau *et al.*, 2001; Trotignon *et al.*,
 226 2010; Blagau *et al.*, 2013, 2014]. The results of these calibrations can appear as sudden
 227 non-physical jumps in the CIS HIA data. The CIS HIA had different modes to measure
 228 in the solar wind and the magnetosphere. When the instrument is switched from one mode
 229 to another mode non-physical jumps also appear in the measurements. These features
 230 impair the accuracy of data analyses.

231 We remove non-physical jumps from our results using a density determination based
 232 on different principles. We use the spacecraft potential of the Electric Field and Wave
 233 Experiment [EFW ; Gustafsson *et al.*, 1997, 2001] to determine the electron density. This
 234 quantity can be calculated using the empirical density formula

$$n_{EFW} = 200(V_{sc})^{-1.85}, \quad (1)$$

235 where n_{EFW} is the calculated density and V_{sc} is the Cluster EFW spacecraft potential
 236 [Trotignon *et al.*, 2010, 2011]. The EFW and the WHISPER were used for the calibra-
 237 tion of the CIS HIA and the Plasma Electron and Current Experiment [PEACE; John-
 238 stone *et al.*, 1997; Fazakerley *et al.*, 2010a,b]. Both instruments were still working on-
 239 board all Cluster spacecraft. Their stable operation reduced the number of data gaps,
 240 and it also made the data analysis easier.

241 **3 Comparison of measurements to simulation**

242 The parameters saved from the GUMICS–4 simulations and the Cluster SC3 mag-
 243 netic field, solar wind velocity and, density measurements are compared in different re-

244 gions, namely the solar wind, magnetosheath, and magnetosphere via cross-correlation
 245 calculations. The temporal resolution of the simulated Cluster orbit data is mostly five
 246 minutes because the results of the simulations are saved every five minutes [Facsikó *et al.*,
 247 2016]. However, the time difference between points can be more than five minutes at the
 248 boundary of the subintervals, because the length of the simulation intervals is determined
 249 in minutes. To facilitate analysis of the simulation results, all simulation data were in-
 250 terpolated to a one-minute resolution. This method does not provide extra information
 251 to the cross-correlation calculation. The data gaps are eliminated using linear interpo-
 252 lation and extrapolation when the gap is at the start or the end of the selected interval.
 253 The spin resolution (4 s) of Cluster SC3 magnetic field measurements is averaged over
 254 five minutes around (± 150 s) the timestamps of the saved data. Then the averaged data
 255 were interpolated to a one-minute resolution to make the correlation calculations.

256 For the correlation calculation, intervals are selected carefully in the solar wind (see
 257 Section 3.1), the magnetosheath (see Section 3.2), the dayside and the night side mag-
 258 netosphere (see Section 3.3). In these intervals, the parameters did not vary a lot and
 259 we exclude intervals when either Cluster or the virtual probe cross any boundaries. To
 260 compare the B_z magnetic field, V_x solar wind speed and the n_{CIS} and the n_{EFW} curves
 261 we cross-correlate selected intervals. We carefully examine such cases, and remove in-
 262 tervals that are shorter than four hours for the ± 60 minutes correlation calculation, and
 263 intervals with large data gaps from the correlation calculation. Those intervals are also
 264 excluded when the plasma instrument has a calibration error or a change in its record-
 265 ing mode as it moves from the magnetosphere to solar wind (for example). The electron
 266 density is also calculated using Equation 1 and correlated. We want to avoid the cali-
 267 bration errors and sudden non-physical jumps mentioned previously. The correlation re-
 268 sults for the density derived from the electric field potential results do not differ signif-
 269 icantly from those for the top hat plasma instrument, however, the EFW's n_{EFW} ex-
 270 periences no mode changes and it is applicable in the magnetosphere too (in contrast to
 271 the CIS HIA instrument).

272 3.1 Solar wind

273 We use OMNI IMF and solar wind velocity, density, and temperature data as in-
 274 put to the simulation. Comparing parameters obtained from the simulation and the mea-
 275 surements in the solar wind region is especially interesting because the IMF X compo-

276 nent cannot be given to the GUMICS–4 as input [Janhunen *et al.*, 2012; Facskó *et al.*,
277 2016]. However, the magnetic field of the solar wind has an X component in the simu-
278 lations. Additionally, solar wind structures might evolve from the simulation domain bound-
279 ary at $+32 R_E$ to the sub-solar point of the terrestrial bow shock where all OMNI data
280 is shifted. Almost the same solar wind time intervals are used as in Table 1 of Facskó
281 *et al.* [2016]. Although the Cluster instruments were calibrated in 2002, just after launch,
282 there are not many CIS HIA moment observations in 2001 and 2002 (Table 1). Hence,
283 we do not have satisfactory ion plasma data coverage for this year. Additionally, to im-
284 prove the accuracy of the correlation calculation (see below) we omitted intervals (shorter
285 than five hours) and those in which the CIS HIA instrument changed its mode. The Clus-
286 ter fleet is located in the solar wind only from December to May and only for a couple
287 of hours during each orbit near apogee. We double–check whether Cluster SC3 remains
288 in the solar wind in both the simulation and reality. We also check the omnidirectional
289 CIS HIA ion spectra on the Cluster Science Archive (CSA; <https://www.cosmos.esa.int/web/csa/csdss-quicklook-plots>). The spectra must contain one narrow band in the solar wind region,
290 indicating an observation of the solar wind beam. Hence, there are only 17 solar wind
291 intervals to study, as shown in Figure 1.

293 The selected intervals occur for quiet solar wind conditions (Figure 2). The GUMICS–4
294 simulation results have five–minute time resolution and the Cluster SC3 measurements
295 have one–minute time resolution (Figure 3). The measurements vary significantly. De-
296 spite the quiet conditions the observed solar wind density often changes and deviates from
297 the simulation. Figure 4c shows that both densities deviate significantly. The CIS HIA
298 density variations are even larger as expected given the complexity and a large number
299 of working modes of the CIS instrument. The magnetic field and the solar wind veloc-
300 ity fit better. Figure 5a shows that the correlation of the magnetic fields is very good;
301 furthermore on Figure 5c, 5e, 5g the correlation of the solar wind velocity and density
302 is excellent (Table 1). The time shift in Figure 5b, Figure 5d, Figure 5f is about five–
303 minutes for the magnetic field and the CIS data. In Figure 5h for the EFW data, the
304 time–shift is less stable. It is not as well determined as in the case of the other param-
305 eters.

306 **3.2 Magnetosheath**

307 Cluster SC3 spent only a little time in the solar wind from December 2002 to May
 308 2003. However, the spacecraft enters the magnetosheath in each orbit (Figure 6). We
 309 select intervals when the value of the magnetic field is around 25 nT. The field should
 310 be fluctuating because of the turbulent deflected flow of the shocked solar wind the tem-
 311 perature should be greater than that in the solar wind. The velocity should decrease to
 312 values ranging from 100-300 km/s. The density of the plasma should increase and reach
 313 values of 10-20 cm⁻³. The narrow band on the omnidirectional CIS HIA ion spectra from
 314 the CSA (<https://www.cosmos.esa.int/web/csa/csds-quicklook-plots>) widens from the
 315 solar wind to the magnetosheath. 15–30 minutes from each bow shock crossing we con-
 316 sidered the Cluster SC3 to have entered into the magnetosheath. At the inner magne-
 317 topause boundary of the magnetopause the flow speed and the density drop. The mag-
 318 netic field strength increases and the magnetic field becomes less turbulent than in the
 319 magnetosheath. The wide band in the omnidirectional CIS HIA ion spectra disappears,
 320 indicating the plasma has undergone heating. 15-30 minutes before (or after) the appear-
 321 ance of these indicators of the magnetopause crossing our intervals end. All intervals con-
 322 taining large data gaps, non-physical jumps in instrument modes or lasting less than four
 323 hours are removed. Hence, 74 intervals considered in our final selection (Table 2).

324 All intervals have quiet upstream (or input) solar wind conditions (Figure 7). De-
 325 spite our selected quiet magnetic field and plasma parameters, the calculated empirical
 326 density indicate that they vary significantly stronger than in the solar wind intervals (Fig-
 327 ure 8). The deviation between the simulated and the observed data is also larger in this
 328 region than in the solar wind region. The scatter plots of the magnetic field, plasma flow
 329 speed, and the densities show that these parameters agree well, but with a greater vari-
 330 ation than the scatter plots for the same parameters in the solar wind (Figure 9a, 9b, 9c).
 331 The correlation of the simulated and the observed data is good for the magnetic field (Fig-
 332 ure 10a), very good for the ion plasma moments and the calculated density (Figure 10c,
 333 10e, 10g). The timeshift of the magnetic field is within five minutes mostly (Figure 10b)
 334 however the timeshift of the ion plasma moments is scattered (Figure 10d, 10f). The timeshift
 335 of the calculated EFW density seems to be more stable (Figure 10h). Generally, the GUMICS-4
 336 is less accurate in the magnetosheath than in the solar wind. The modeled magnetic field
 337 is better predicted than the modeled plasma parameters are. The calculated empirical
 338 EFW density (n_{EFW}) fits better than the CIS HIA density (n_{CIS}).

339 **3.3 Magnetosphere**

340 We select intervals in the magnetosphere based on the CIS HIA omnidirectional
 341 ion flux spectrum. The magnetosphere is defined by the disappearance of hot magne-
 342 tosheath ion population. The plasma density decreases toward zero, the magnetic field
 343 strength becomes great. We eliminated 15–30 min after/before the magnetopause trans-
 344 ition to identify magnetosphere intervals. This way we found 132 intervals of which we
 345 found 132 (Table 3) using Cluster SC3 measurements. Cluster SC3 spends considerable
 346 time in the magnetosphere (Figure 11).

347 Here we show neither any correlation calculation nor comparison plot. In the mag-
 348 netosphere, the GUMICS–4 does not work well. Neither the magnetic field nor the plasma
 349 moments nor the N_{EFW} fit well. The solar wind velocity does not reach zero in the sim-
 350 ulation. Instead, the solar wind enters the night side magnetosphere. The solar wind CIS
 351 HIA ion plasma density and the calculated density from spacecraft potential increase closer
 352 to the Earth (plasmasphere). The GUMICS–4 density is low there. We calculated the
 353 dipole field in GSE using Tsyganenko Geotool box [Tsyganenko, 1995] and subtracted
 354 from both the observed and the simulated magnetic field B_z data. The correlation of these
 355 corrected magnetic field measurements and simulations is very low too.

356 **3.4 Bow shock, magnetopause, neutral sheet locations**

357 We selected 77 intervals when Cluster SC3 crossed the terrestrial bow shock once
 358 or multiple times (Table 4). When the spacecraft crosses the bow shock inbound the mag-
 359 nitude of the magnetic field and the solar wind density increases by a factor to 4–5 (from
 360 5 nT or 5 cm^{-3} , respectively), the solar wind speed drops from 400–600 km/s to 100–300 km/s;
 361 furthermore the narrow band in the omnidirectional Cluster CIS HIA ion spectra widens.
 362 Both the Cluster measurements and the GUMICS–4 simulations have 5-min resolution
 363 and are interpolated to 1-min resolution. All bow shock transitions of the virtual space-
 364 craft are slower and smoother. Additionally, GUMICS-4 does not predict multiple bow
 365 shock transitions. The code reacts slowly to such sudden changes. The magnetic signa-
 366 tures fit better than the calculated plasma moments. The jump of the ion plasma pa-
 367 rameters and the derived Cluster EFW density of the simulations are shifted to the mea-
 368 surements. Generally, the density and the velocity of the simulations seem to be less ac-
 369 curate than the magnetic field in the simulations.

54 intervals are selected around magnetopause crossings (Table 5). When the space-craft crosses the magnetopause inbound the magnitude of the magnetic field increases, the solar wind speed drops from 100–300 km/s to zero, the plasma density becomes zero; furthermore the wide band on the omnidirectional Cluster CIS HIA ion spectra disappears. The location of the magnetopause is well determined by the Cluster SC3 measurements. However, it is very difficult to identify the magnetopause crossings in the simulation data. The magnetopause crossings usually (92 %) cannot be seen in the simulations. The magnetopause crossings are not visible in V_x and n . This observation is independent of the IMF orientation. Or when the magnetopause crossings are identified in both simulations and spacecraft measurements the events are shifted in time and location. The accuracy of the model is lower for the dayside magnetopause locations than the bow shock locations.

Nine intervals are chosen around Cluster SC3 neutral sheet crossings (Figure 12; Table 6). The neutral sheet locations are determined using the results of the Boundary Layer Identification Code (BLIC) Project [Facsikó *et al.*, in preparation]. The BLIC code determines the neutral sheet crossing Cluster FGM magnetic field measurements using Wang and Xu [1994]’s method. When the solar wind speed is very low around the currents sheet in the simulation space; furthermore the CIS HIA density and the EFW calculated density are very low near the current sheet too; finally the GSE Z component of the magnetic field changing is a sign of the code–indicated neutral sheet crossing (Figure 13; red and blue curves). The neutral sheet crossings are visible in the GUMICS simulations (Figure 13; black curves). For five events (from nine Cluster SC3 crossings) the GUMICS–4 also provides similar smoothed parameters and change of sign of the B_z component. This is an outstanding result because the tail in the GUMICS–4 simulations is significantly smaller than observed in reality [Gordeev *et al.*, 2013; Facsikó *et al.*, 2016]; furthermore the solar wind enters the tail in MHD simulations generally [Kallio and Facsikó, 2015].

4 Discussion

The agreement of B_z , V_x and n_{EFW} in the solar wind with the similar GUMICS simulation predictions is very good (Figure 4a, 4b, 4c, blue). The agreement of n_{CIS} is worse (Figure 4c, red). It was expected because the n_{EFW} depends on the spacecraft potential provided by the EFW instrument. However, the CIS instrument has many modes

for measuring the plasma parameters and it needs periodic calibration too. The correlation of the solar wind V_x , n_{CIS} and n_{EFW} with the similar GUMICS simulation parameters is greater than 0.9 (Figure 5c, 5e, 5g). The correlation of the B_z is also greater than 0.8 (Figure 5a). The upstream boundary of the GUMICS–4 code lies at $32 R_E$ [Jan-hunen *et al.*, 2012], the nose of the terrestrial bow shock is at about $20 R_E$. If the solar wind speed is 400 km/s, then this spatial distance means less than a 5 minutes delay, so it should not be visible in the time delays from the cross-correlations. 80% of the intervals support this theory but 20% do not. In these cases, the one-minute resolution B_z , n_{CIS} or the n_{EFW} parameters have a sudden jump or variation that the simulation cannot follow, or the resolution of the simulation output (5 minutes) is too small to see these variations. Therefore, the correlation calculation is not accurate in these cases. Previously the OMNI data was compared to the Cluster data and the Cluster measurements were compared to the GUMICS–4 [Facsikó *et al.*, 2016]. The comparison suggests that the GUMICS–4 results should be similar to the OMNI data. Furthermore, we calculate correlation functions in the solar wind, where there is no significant perturbation of the input parameters in the simulation box. Therefore, we get the expected result after comparing the two different correlation calculations.

In the magnetosheath we get worse agreement with the GUMICS simulation data (Figure 9a, 9b, 9c). While the parameters are correlated, the scatter is greater. The general reason for this larger uncertainty seems to be that the magnetosheath is turbulent. This phenomenon explains the higher variations of the B_z magnetic field on Figure 9a. The solar wind V_x , n_{CIS} and n_{EFW} agree better than the magnetic field component (Figure 9b, 9c). Here there is no deviation between the densities derived in different ways (n_{CIS} and n_{EFW}) on Figure 9c. Figure 10 seems to contradict these statements above. The larger uncertainty of the B_z is visible in Figure 10a. However, that correlation is still good in Figure 10b. The other parameters have larger (> 0.9) correlation in Figure 10c, 10e, 10g. However, the time shifts in Figure 10d, 10f, 10h seem to be worse. Here the time shifts are worse because the shape of the time series in the magnetosheath looks very smooth and similar hence there are not enough points to get a sharp and large maximum correlation as the function of timeshift. The difference between the minimum and the maximum of the correlation is small compared with the uncertainty of the calculation. The maximum, the timeshift could be anywhere and the shape of the correlation vs. timeshift function is often neither symmetric nor does it have only one local max-

435 imum. Hence, the correlation calculation provides larger time shifts for the ion plasma
 436 parameters and the n_{EFW} .

437 In the magnetosphere, the GUMICS–4 does not work well. GUMICS–4 uses a tilted
 438 dipole to describe the terrestrial magnetic field [Janhunen *et al.*, 2012]. After removing
 439 the magnetic dipole from the magnetic field measurements of the Cluster SC3 and the
 440 simulation we get very low correlations and unacceptable time shifts (not shown). The
 441 tilted dipole is an insufficient description of the inner magnetospheric magnetic field. The
 442 plasma moments and the n_{EFW} do not fit either. The single fluid, ideal MHD does not
 443 describe the inner magnetosphere well therefore V_x and n in the simulations do not agree
 444 with V_x , n_{CIS} and the n_{EFW} measured by the Cluster SC3. Within the $3.7 R_E$ domain
 445 ring current physics must be added, as it has been in other global MHD codes [for ex-
 446 ample Tóth *et al.*, 2012]. This can explain the limited accuracy of the cross–polar cap
 447 potential (CPCP) and geomagnetic indices of the GUMICS simulations [Juusola *et al.*,
 448 2014]. The CPCP GUMICS agrees well with spacecraft measurements therefore this quan-
 449 tity could be used for simulation studies [Lakka *et al.*, 2018a]. Haiduček *et al.* [2017] also
 450 compared geomagnetic indices and the CPCP. The Space Weather Modelling Framework
 451 (SWMF) was tested. When the inner magnetosphere model was switched off in the sim-
 452 ulation only the comparison of the simulated and observed CPCP was good. Therefore,
 453 the reason for the discrepancy of the geomagnetic indices in the GUMICS simulations
 454 must be the missing inner magnetosphere model.

455 The reason why simulation results and measurements disagree could be the code
 456 or bad input parameters. During the 1-year run the distributions of the OMNI solar wind
 457 magnetic field B_x , B_y , B_z components; solar wind velocity V_x , V_y , V_z components and
 458 the solar wind P dynamic pressure are calculated from January 29, 2002 to February 2,
 459 2003 in GSE reference frame. The distributions of the OMNI solar wind magnetic field
 460 B_x , B_y , B_z components were overplotted by red in Figure 14a, 14d, 14g, 14j and Fig-
 461 ure 17a, 17d, 17g, 17j; Figure 14b, 14e, 14h, 14k and Figure 17b, 17e, 17h, 17k; further-
 462 more Figure 14c, 14f, 14i, 14l and Figure 17c, 17f, 17i, 17l. The distributions of the OMNI
 463 solar wind velocity V_x , V_y , V_z components were overplotted by red in Figure 15a, 15d, 15g, 15j
 464 and Figure 18a, 18d, 18g, 18j; Figure 15b, 15e, 15h, 15k and Figure 18b, 18e, 18h, 18k;
 465 furthermore Figure 15c, 15f, 15i, 15l and Figure 18c, 18f, 18i, 18l. The distributions of
 466 the P solar wind pressure calculated from the OMNI solar wind parameters were over-
 467 plotted by red in Figure 16a, 16b, 16c, 16d and Figure 19a, 19b, 19c, 19d. The intervals

when the GUMICS–4 simulations and the Cluster SC3 measurements disagreed are collected for intervals in the solar wind (Table 7) and the magnetosheath (Table 8). The definition of disagreement of the simulations and measurements is quite arbitrary. When the two curves deviate or the correlation function is not symmetric we considered the simulations and the measurements disagreeing. The correlation coefficients are also high in these cases however the time shift is large (~ 60 min). The averaged shifted OMNI parameters of the poorly agreeing intervals from the Tables 7 and 8 are saved. The distributions of the OMNI parameters belonging to the bad simulation results are calculated for the solar wind region (Figure 14, 15 and 16) and in the magnetosheath (Figure 17, 18 and 19).

1. In the solar wind the distributions of the OMNI B_x , B_y and B_z can be compared in Figure 14a, 14d, 14g, 14j; Figure 14b, 14e, 14h, 14k; furthermore in Figure 14c, 14f, 14i, 14l.
 - (a) When the B_z disagrees in simulations and measurements in Figure 14a, 14b, 14c the black and red distributions of the OMNI B_x , B_y and B_z are not similar. The reason for these strange spikes is that there is only one poorly correlated interval for the B_z in the solar wind according to Table 7.
 - (b) When the V_x disagrees in simulations and measurements in Figure 14d, 14e, 14f the black and red distributions of the OMNI B_x , B_y and B_z are similar. The distributions do not agree perfectly because in Table 7 the number of the poorly correlated intervals is only six for the V_x component.
 - (c) When the n_{CIS} disagrees in simulations and measurements in Figure 14g, 14h, 14i the black and red distributions of the OMNI B_x , B_y and B_z are similar. The distributions do not agree perfectly because in Table 7 the number of the poorly correlated intervals is only twelve for the n_{CIS} .
 - (d) When the n_{EFW} disagrees in Figure 14j, 14k, 14l the black and red distributions of the OMNI B_x , B_y and B_z are similar. The distributions do not agree perfectly because in Table 7 the number of the poorly correlated intervals is only nine for n_{EFW} .

The values of the OMNI B_x , B_y , and B_z are not peculiar in the solar wind.

2. In the solar wind the distributions of the OMNI V_x , V_y and V_z can be compared in Figure 15a, 15d, 15g, 15j; Figure 15b, 15e, 15h, 15k; furthermore in Figure 15c, 15f, 15i, 15l.
 - (a) When the B_z disagrees in Figure 15a, 15b, 15c the black and red distributions of the OMNI V_x , V_y and V_z are not similar. The reason for these strange spikes

500 is that there is only one poorly correlated interval for the B_z in the solar wind
 501 according to Table 7.

- 502 (b) When the V_x disagrees in simulations and measurements in Figure 15d, 15e, 15f
 503 the black and red distributions of the OMNI V_x , V_y and V_z are similar. The dis-
 504 tributions do not agree perfectly because in Table 7 the number of the poorly
 505 correlated intervals is only six for the V_x component.
- 506 (c) When the n_{CIS} disagrees in Figure 15g, 15h, 15i the black and red distributions
 507 of the OMNI V_x , V_y and V_z are similar. The distributions do not agree perfectly
 508 because in Table 7 the number of the poorly correlated intervals is only twelve
 509 for the n_{CIS} .
- 510 (d) When the n_{EFW} disagrees in simulations and measurements in Figure 15j, 15k, 15l
 511 the black and red distributions of the OMNI V_x , V_y and V_z are similar. The dis-
 512 tributions do not agree perfectly because in Table 7 the number of the poorly
 513 correlated intervals is only nine for the n_{EFW} .

514 The values of the OMNI V_x , V_y , and V_z are not peculiar in the solar wind.

515 3. In the solar wind the distributions of the solar wind P calculated from OMNI pa-
 516 rameters can be compared in Figure 16a, 16b, 16c, 16d.

- 517 (a) When the B_z disagrees in Figure 16a the black and red distributions of the OMNI
 518 P are not similar. The reason for this strange spike is that there is only one poorly
 519 correlated interval for the B_z in the solar wind according to Table 7.
- 520 (b) When the V_x disagrees in simulations and measurements in Figure 16b the black
 521 and red distributions of the OMNI P are similar. The distributions do not agree
 522 perfectly because in Table 7 the number of the poorly correlated intervals is only
 523 six V_x component.
- 524 (c) When the n_{CIS} disagrees in simulations and measurements in Figure 16c the
 525 black and red distributions of the OMNI P are similar. The distributions do
 526 not agree perfectly because in Table 7 the number of the poorly correlated in-
 527 tervals is only twelve for the n_{CIS} .
- 528 (d) When the n_{EFW} disagrees in simulations and measurements in Figure 16d the
 529 black and red distributions of the OMNI P are similar. The distributions do
 530 not agree perfectly because in Table 7 the number of the poorly correlated in-
 531 tervals is only nine for the n_{EFW} .

532 The values of the OMNI P are not peculiar in the solar wind.

533 4. In the magnetosheath the distributions of the OMNI B_x , B_y and B_z can be com-
 534 pared in Figure 17a, 17d, 17g, 17j; Figure 17b, 17e, 17h, 17k; furthermore in Fig-
 535 ure 17c, 17f, 17i, 17l.

536 (a) When the B_z disagrees in simulations and measurements in Figure 17a, 17b, 17c
 537 the black and red distributions of the OMNI B_x , B_y and B_z are similar.

538 (b) When the V_x disagrees in simulations and measurements in Figure 17d, 17e, 17f
 539 the black and red distributions of the OMNI B_x , B_y and B_z are similar.

540 (c) When the n_{CIS} disagrees in simulations and measurements in Figure 17g, 17h, 17i
 541 the black and red distributions of the OMNI B_x , B_y and B_z are similar.

542 (d) When the n_{EFW} disagrees in Figure 17j, 17k, 17l the black and red distribu-
 543 tions of the OMNI B_x , B_y and B_z are similar.

544 The distributions agree quite well because in Table 8 the number of the poorly
 545 correlated intervals 18, 50, 33 and 30 for the B_z , the V_x , the n_{CIS} and n_{CIS} com-
 546 ponents, respectively. The number of cases is higher and the values of the OMNI
 547 B_x , B_y and B_z are not peculiar in the magnetosheath.

548 5. In the magnetosheath the distributions of the OMNI V_x , V_y and V_z can be com-
 549 pared in Figure 18a, 18d, 18g, 18j; Figure 18b, 18e, 18h, 18k; furthermore in Fig-
 550 ure 18c, 18f, 18i, 18l.

551 (a) When the B_z disagrees in Figure 18a, 18b, 18c the black and red distributions
 552 of the OMNI V_x , V_y and V_z are similar.

553 (b) When the V_x disagrees in simulations and measurements in Figure 18d, 18e, 18f
 554 the black and red distributions of the OMNI V_x , V_y and V_z are similar.

555 (c) When the n_{CIS} disagrees in Figure 18g, 18h, 18i the black and red distributions
 556 of the OMNI V_x , V_y and V_z are similar.

557 (d) When the n_{EFW} disagrees in simulations and measurements in Figure 18j, 18k, 18l
 558 the black and red distributions of the OMNI V_x , V_y and V_z are similar.

559 The distributions agree quite well because in Table 8 the number of the poorly
 560 correlated intervals 18, 50, 33 and 30 for the B_z , the V_x , the n_{CIS} and n_{CIS} com-
 561 ponents, respectively. The number of cases is higher and the values of the OMNI
 562 V_x , V_y and V_z are not peculiar in the magnetosheath.

- 563 6. In the magnetosheath the distributions of the solar wind P calculated from OMNI
 564 parameters can be compared in Figure 19a, 19b, 19c, 19d.
- 565 (a) When the B_z disagrees in Figure 19a the black and red distributions of the OMNI
 566 P are similar.
- 567 (b) When the V_x disagrees in simulations and measurements in Figure 19b the black
 568 and red distributions of the OMNI P are similar.
- 569 (c) When the n_{CIS} disagrees in simulations and measurements in Figure 19c the
 570 black and red distributions of the OMNI P are similar.
- 571 (d) When the n_{EFW} disagrees in simulations and measurements in Figure 19d the
 572 black and red distributions of the OMNI P are similar.

573 The distributions agree quite well because in Table 8 the number of the poorly
 574 correlated intervals 18, 50, 33 and 30 for the B_z , the V_x , the n_{CIS} and n_{CIS} com-
 575 ponents, respectively. The number of cases is higher and the values of the OMNI
 576 P are not peculiar in the magnetosheath.

577 The inaccuracy of the GUMICS-4 simulations does not depend on the OMNI parame-
 578 ters in the solar wind and magnetosheath regions. The same study does not need to be
 579 done for the magnetosphere because the deviation of the measurements and the simu-
 580 lations is so large that it cannot be caused by wrong OMNI solar wind parameters.

581 The bow shock positions agree in the GUMICS simulations and the Cluster SC3
 582 measurements. However, the magnetopause locations do not match as well as the bow
 583 shock in simulations and observations. In simulations the location of the magnetopause
 584 is determined from peaks in currents density, particle density gradient, or changes in flow
 585 velocity [Siscoe *et al.*, 2001; García and Hughes, 2007; Gordeev *et al.*, 2013, see references
 586 therein]. Here the previously saved simulation parameters along the virtual Cluster SC3
 587 orbit are analyzed. The J_y current density component cannot readily be determined from
 588 measurements by a single spacecraft. Therefore, the above-mentioned methods cannot
 589 be applied. This discrepancy of the magnetopause location agrees with the results of Gordeev
 590 *et al.* [2013] and Facskó *et al.* [2016]. Gordeev *et al.* [2013] compared synthetic GUMICS
 591 runs with an empirical formula for the magnetopause locations. Facskó *et al.* [2016] used
 592 OMNI solar wind data as input and got the same result as Gordeev *et al.* [2013] and this
 593 paper. The neutral sheets are visible in both simulations and observations (Figure 13, Ta-
 594 ble 6). This experience is exceptional because the night side magnetosphere of the GUMICS-4

595 simulations is small and twisted [*Gordeev et al.*, 2013; *Facskó et al.*, 2016]. However, in
 596 these cases, the IMF has no large B_y component. From *Facskó et al.* [2016] we know that
 597 the GUMICS has a normal long tail (or night side magnetosphere) if the B_y is small. The
 598 code can identify the bow shock transitions. For the magnetopause and the neutral sheet,
 599 the results are more complex.

600 5 Summary and conclusions

601 Based on the previously created 1-year long GUMICS–4 run global MHD simu-
 602 lation results are compared with Cluster SC3 magnetic field, solar wind velocity, and den-
 603 sity measurements along the spacecraft orbit. Intervals are selected when the Cluster SC3
 604 and the virtual space probe are situated in the solar wind, magnetosheath, and magne-
 605 tosphere; furthermore their correlation is calculated. Bow shock, magnetopause, and neu-
 606 tral sheet crossings are selected and their visibility and relative position are compared.
 607 We achieved the following results:

- 608 1. In the solar wind the correlation coefficient of the B_z , the V_x , the n_{EFW} and the
 609 n_{CIS} are larger than 0.8, 0.9, 0.9 and 0.9, respectively. The agreement of the B_z ,
 610 the V_x , and the n_{EFW} is very good, furthermore the agreement of the n_{CIS} is also
 611 good.
- 612 2. In the magnetosheath the correlation coefficient of the B_z , the V_x , the n_{EFW} and
 613 the n_{CIS} are larger than 0.6, 0.9, 0.9 and 0.9, respectively. The agreement of the
 614 magnetic field component, the ion plasma moments, and the calculated empiri-
 615 cal density is a bit weaker than in the solar wind. The V_x , the n_{EFW} and the n_{CIS}
 616 fits better than the B_z component in the magnetosheath. Their agreement is still
 617 good. The reason for the deviation is the turbulent behavior of the slowed down
 618 and thermalized turbulent solar wind.
- 619 3. In neither the dayside nor the nightside magnetosphere can the GUMICS–4 pro-
 620 vide realistic results. The simulation outputs and the spacecraft measurement dis-
 621 agree in this region. The reason for this deviation must be the missing coupled
 622 inner magnetosphere model. The applied tilted dipole approach is not satisfac-
 623 tory in the magnetosphere at all.
- 624 4. Disagreement between GUMICS–4 and observations does not seem to be due to
 625 any particular upstream solar wind conditions.

626 5. The position of the bow shock and the neutral sheet agrees well in the simulations
 627 and the Cluster SC3 magnetic field, ion plasma moments, and derived electron den-
 628 sity measurements in this study. The position of the magnetopause does not fit
 629 that well.

630 The GUMICS–4 has scientific and strategic importance for the European Space Weather
 631 and Scientific community. This code developed in the Finnish Meteorological Institute
 632 is the most developed and tested, widely used tool for modeling the cosmic environment
 633 of the Earth in Europe. An inner magnetosphere model should be two-way coupled to
 634 the existing configuration of the simulation tool to improve the accuracy of the simu-
 635 lations.

636 Acknowledgments

637 The OMNI data were obtained from the GSFC/SPDF OMNIWeb interface at <http://omniweb.gsfc.nasa.gov>.
 638 The authors thank the FGM Team (PI: Chris Carr), the CIS Team (PI: Iannis Dandouras),
 639 the WHISPER Team (PI: Jean-Louis Rauch), the EFW Team (PI: Mats Andre), and
 640 the Cluster Science Archive for providing FGM magnetic field, CIS HIA ion plasma and
 641 WHISPER electron density measurements. Data analysis was partly done with the QSAS
 642 science analysis system provided by the United Kingdom Cluster Science Centre (Im-
 643 perial College London and Queen Mary, University of London) supported by the Science
 644 and Technology Facilities Council (STFC). Eija Tanskanen acknowledges financial sup-
 645 port from the Academy of Finland for the ReSoLVE Centre of Excellence (project No. 272157).
 646 Gábor Facskó thanks Anna-Mária Vigh for improving the English of the paper. The au-
 647 thors thank Pekka Janhunen for developing the GUMICS–4 code; furthermore, Minna
 648 Palmroth and Zoltán Vörös for the useful discussions. The work of Gábor Facskó was
 649 supported by mission science funding for the Van Allen Probes mission, the American
 650 Geophysical Union, and the Institute of Earth Physics and Space Science (ELKH EPSS),
 651 Sopron, Hungary. For further use of the year run data, request the authors or use the
 652 archive of the Community Coordinated Modelling Center (https://ccmc.gsfc.nasa.gov/publications/posted_runs/).

653

654 References

655 Balogh, A., M. W. Dunlop, S. W. H. Cowley, D. J. Southwood, J. G. Thomlinson,
 656 K. H. Glassmeier, G. Musmann, H. Luhr, S. Buchert, M. H. Acuna, D. H. Fair-

- field, J. A. Slavin, W. Riedler, K. Schwingenschuh, and M. G. Kivelson (1997), The Cluster Magnetic Field Investigation, *Space Science Reviews*, 79, 65–91, doi: 10.1023/A:1004970907748.
- Balogh, A., C. M. Carr, M. H. Acuña, M. W. Dunlop, T. J. Beek, P. Brown, K. Fornaçon, E. Georgescu, K. Glassmeier, J. Harris, G. Musmann, T. Oddy, and K. Schwingenschuh (2001), The Cluster Magnetic Field Investigation: overview of in-flight performance and initial results, *Annales Geophysicae*, 19, 1207–1217.
- Bartels, J., N. H. Heck, and H. F. Johnston (1939), The three-hour-range index measuring geomagnetic activity, *Terrestrial Magnetism and Atmospheric Electricity (Journal of Geophysical Research)*, 44, 411, doi:10.1029/TE044i004p00411.
- Blagau, A., I. Dandouras, A. Barthe, S. Brunato, G. Facskó, and V. Constantinescu (2013), In-flight calibration of Hot Ion Analyser onboard Cluster, *Geoscientific Instrumentation, Methods and Data Systems Discussions*, 3, 407–435, doi:10.5194/gid-3-407-2013.
- Blagau, A., I. Dandouras, A. Barthe, S. Brunato, G. Facskó, and V. Constantinescu (2014), In-flight calibration of the Hot Ion Analyser on board Cluster, *Geoscientific Instrumentation, Methods and Data Systems*, 3, 49–58, doi:10.5194/gi-3-49-2014.
- Chittenden, J. P., S. V. Lebedev, C. A. Jennings, S. N. Bland , and A. Ciardi (2004), X-ray generation mechanisms in three-dimensional simulations of wire array Z-pinches, *Plasma Physics and Controlled Fusion*, 46(12B), B457–B476, doi:10.1088/0741-3335/46/12B/039.
- Ciardi, A., S. V. Lebedev, A. Frank, E. G. Blackman, J. P. Chittenden, C. J. Jennings, D. J. Ampleford, S. N. Bland, S. C. Bott, J. Rapley, G. N. Hall, F. A. Suzuki-Vidal, A. Marocchino, T. Lery, and C. Stehle (2007), The evolution of magnetic tower jets in the laboratory, *Physics of Plasmas*, 14(5), 056,501–056,501, doi:10.1063/1.2436479.
- Credland, J., G. Mecke, and J. Ellwood (1997), The Cluster Mission: ESA'S Spacefleet to the Magnetosphere, *Space Science Reviews*, 79, 33–64, doi: 10.1023/A:1004914822769.
- Davis, T. N., and M. Sugiura (1966), Auroral electrojet activity index AE and its universal time variations, *Journal of Geophysical Research*, 71, 785–801, doi: 10.1029/JZ071i003p00785.

- 690 Décréau, P. M. E., P. Fergeau, V. Krasnoselskikh, E. Le Guiriec, M. Lévéque,
691 P. Martin, O. Randriamboarison, J. L. Rauch, F. X. Sené, H. C. Séran, J. G.
692 Trotignon, P. Canu, N. Cornilleau, H. de Féraudy, H. Alleyne, K. Yearby, P. B.
693 Mögensen, G. Gustafsson, M. André, D. C. Gurnett, F. Darrouzet, J. Lemaire,
694 C. C. Harvey, P. Travnicek, and Whisper Experimenters Group (2001), Early re-
695 sults from the Whisper instrument on Cluster: an overview, *Annales Geophysicae*,
696 *19*, 1241–1258, doi:10.5194/angeo-19-1241-2001.
- 697 Escoubet, C. P., M. Fehringer, and M. Goldstein (2001), Introduction The Cluster
698 mission, *Annales Geophysicae*, *19*, 1197–1200, doi:10.5194/angeo-19-1197-2001.
- 699 Facskó, G., I. Honkonen, T. Živković, L. Palin, E. Kallio, K. Ågren, H. Opgenoorth,
700 E. I. Tanskanen, and S. Milan (2016), One year in the Earth’s magnetosphere: A
701 global MHD simulation and spacecraft measurements, *Space Weather*, *14*, 351–
702 367, doi:10.1002/2015SW001355.
- 703 Facskó, G., T. B. Balogh, E. I. Anekallu, C. R. and Tanskanen, P. Peitso, L. Degener,
704 M. Kangwa, T. Laitinen, and S. Laakso, H. Burley (in preparation), Bow shock
705 identification in cluster measurements, *Space Weather*.
- 706 Fazakerley, A. N., A. D. Lahiff, R. J. Wilson, I. Rozum, C. Anekallu, M. West, and
707 H. Bacai (2010a), PEACE Data in the Cluster Active Archive, *Astrophysics and
708 Space Science Proceedings*, *11*, 129–144, doi:10.1007/978-90-481-3499-1_8.
- 709 Fazakerley, A. N., A. D. Lahiff, I. Rozum, D. Kataria, H. Bacai, C. Anekallu,
710 M. West, and A. Åsnes (2010b), Cluster-PEACE In-flight Calibration Status,
711 *Astrophysics and Space Science Proceedings*, *11*, 281–299, doi:10.1007/978-90-481-
712 3499-1_19.
- 713 García, K. S., and W. J. Hughes (2007), Finding the Lyon-Fedder-Mobarry mag-
714 netopause: A statistical perspective, *Journal of Geophysical Research (Space
715 Physics)*, *112*(A6), A06229, doi:10.1029/2006JA012039.
- 716 Gordeev, E., G. Facskó, V. Sergeev, I. Honkonen, M. Palmroth, P. Janhunen, and
717 S. Milan (2013), Verification of the GUMICS-4 global MHD code using empirical
718 relationships, *Journal of Geophysical Research (Space Physics)*, *118*, 3138–3146,
719 doi:10.1002/jgra.50359.
- 720 Greenwald, R. A., K. B. Baker, J. R. Dudeney, M. Pinnock, T. B. Jones, E. C.
721 Thomas, J.-P. Villain, J.-C. Cerisier, C. Senior, C. Hanuise, R. D. Hunsucker,
722 G. Sofko, J. Koehler, E. Nielsen, R. Pellinen, A. D. M. Walker, N. Sato,

- 723 and H. Yamagishi (1995), Darn/Superdarn: A Global View of the Dynam-
724 ics of High-Latitude Convection, *Space Science Reviews*, 71, 761–796, doi:
725 10.1007/BF00751350.
- 726 Guild, T. B., H. E. Spence, E. L. Kepko, V. Merkin, J. G. Lyon, M. Wiltberger, and
727 C. C. Goodrich (2008a), Geotail and LFM comparisons of plasma sheet clima-
728 tology: 1. Average values, *Journal of Geophysical Research (Space Physics)*, 113,
729 A04216, doi:10.1029/2007JA012611.
- 730 Guild, T. B., H. E. Spence, E. L. Kepko, V. Merkin, J. G. Lyon, M. Wiltberger, and
731 C. C. Goodrich (2008b), Geotail and LFM comparisons of plasma sheet climatol-
732 ogy: 2. Flow variability, *Journal of Geophysical Research (Space Physics)*, 113,
733 A04217, doi:10.1029/2007JA012613.
- 734 Gustafsson, G., R. Bostrom, B. Holback, G. Holmgren, A. Lundgren, K. Stasiewicz,
735 L. Ahlen, F. S. Mozer, D. Pankow, P. Harvey, P. Berg, R. Ulrich, A. Pedersen,
736 R. Schmidt, A. Butler, A. W. C. Fransen, D. Klinge, M. Thomsen, C.-G. Faltham-
737 mar, P.-A. Lindqvist, S. Christenson, J. Holtet, B. Lybekk, T. A. Sten, P. Tan-
738 skanen, K. Lappalainen, and J. Wygant (1997), The Electric Field and Wave
739 Experiment for the Cluster Mission, *Space Science Reviews*, 79, 137–156, doi:
740 10.1023/A:1004975108657.
- 741 Gustafsson, G., M. André, T. Carozzi, A. I. Eriksson, C.-G. Fälthammar, R. Grard,
742 G. Holmgren, J. A. Holtet, N. Ivchenko, T. Karlsson, Y. Khotyaintsev, S. Klimov,
743 H. Laakso, P.-A. Lindqvist, B. Lybekk, G. Marklund, F. Mozer, K. Mursula,
744 A. Pedersen, B. Popielawska, S. Savin, K. Stasiewicz, P. Tanskanen, A. Vaivads,
745 and J.-E. Wahlund (2001), First results of electric field and density observations
746 by Cluster EFW based on initial months of operation, *Annales Geophysicae*, 19,
747 1219–1240, doi:10.5194/angeo-19-1219-2001.
- 748 Haiducek, J. D., D. T. Welling, N. Y. Ganushkina, S. K. Morley, and D. S. Oz-
749 turk (2017), SWMF Global Magnetosphere Simulations of January 2005: Geo-
750 magnetic Indices and Cross-Polar Cap Potential, *Space Weather*, 15, 1567–1587,
751 doi:10.1002/2017SW001695.
- 752 Iyemori, T. (1990), Storm-time magnetospheric currents inferred from mid-latitude
753 geomagnetic field variations, *Journal of Geomagnetism and Geoelectricity*, 42,
754 1249–1265, doi:10.5636/jgg.42.1249.
- 755 Janhunen, P., M. Palmroth, T. Laitinen, I. Honkonen, L. Juusola, G. Facskó, and

- 756 T. I. Pulkkinen (2012), The GUMICS-4 global MHD magnetosphere-ionosphere
757 coupling simulation, *Journal of Atmospheric and Solar-Terrestrial Physics*, 80,
758 48–59, doi:10.1016/j.jastp.2012.03.006.
- 759 Johnstone, A. D., C. Alsop, S. Burge, P. J. Carter, A. J. Coates, A. J. Coker, A. N.
760 Fazakerley, M. Grande, R. A. Gowen, C. Gurgiolo, B. K. Hancock, B. Narheim,
761 A. Preece, P. H. Sheather, J. D. Winningham, and R. D. Woodliffe (1997), Peace:
762 a Plasma Electron and Current Experiment, *Space Science Reviews*, 79, 351–398,
763 doi:10.1023/A:1004938001388.
- 764 Juusola, L., O. Amm, K. Kauristie, and A. Viljanen (2007), A model for estimating
765 the relation between the Hall to Pedersen conductance ratio and ground magnetic
766 data derived from CHAMP satellite statistics, *Annales Geophysicae*, 25, 721–736,
767 doi:10.5194/angeo-25-721-2007.
- 768 Juusola, L., G. Facskó, I. Honkonen, P. Janhunen, H. Vanhamäki, K. Kauristie,
769 T. V. Laitinen, S. E. Milan, M. Palmroth, E. I. Tanskanen, and A. Viljanen
770 (2014), Statistical comparison of seasonal variations in the GUMICS-4 global
771 MHD model ionosphere and measurements, *Space Weather*, 12, 582–600, doi:
772 10.1002/2014SW001082.
- 773 Kallio, E., and G. Facskó (2015), Properties of plasma near the moon in the magne-
774 total, *Planetary and Space Science*, 115, 69–76, doi:10.1016/j.pss.2014.11.007.
- 775 Kokubun, S., T. Yamamoto, M. H. Acuña, K. Hayashi, K. Shiokawa, and H. Kawano
776 (1994), The GEOTAIL Magnetic Field Experiment., *Journal of Geomagnetism*
777 and *Geoelectricity*, 46, 7–21, doi:10.5636/jgg.46.7.
- 778 Lakka, A., T. I. Pulkkinen, A. P. Dimmock, M. Myllys, I. Honkonen, and M. Palm-
779 roth (2018a), The Cross-Polar Cap Saturation in GUMICS-4 During High Solar
780 Wind Driving, *Journal of Geophysical Research (Space Physics)*, 123, 3320–3332,
781 doi:10.1002/2017JA025054.
- 782 Lakka, A., T. I. Pulkkinen, A. P. Dimmock, E. Kilpua, M. Ala-Lahti, I. Honko-
783 nen, M. Palmroth, and Raukunen (2018b), Icme impact at earth with low and
784 typical mach number plasma characteristics, *Annales Geophysicae Discussions*,
785 <https://doi.org/10.5194/angeo-2018-81>.
- 786 Lani, A., A. Sanna, N. Villedieu, and M. Panesi (2012), COOLFluiD an Open Com-
787 putational Platform for Aerothermodynamics and Flow-Radiation Coupling, in
788 *ESA Special Publication*, *ESA Special Publication*, vol. 714, p. 45.

- 789 Liemohn, M., N. Y. Ganushkina, D. L. De Zeeuw, L. Rastaetter, M. Kuznetsova,
790 D. T. Welling, G. Toth, R. Ilie, T. I. Gombosi, and B. van der Holst (2018), Real-
791 Time SWMF at CCMC: Assessing the Dst Output From Continuous Operational
792 Simulations, *Space Weather*, 16(10), 1583–1603, doi:10.1029/2018SW001953.
- 793 Lyon, J. G., J. A. Fedder, and C. M. Mobarry (2004), The Lyon-Fedder-Mobarry
794 (LFM) global MHD magnetospheric simulation code, *Journal of Atmospheric and*
795 *Solar-Terrestrial Physics*, 66, 1333–1350, doi:10.1016/j.jastp.2004.03.020.
- 796 Mejnertsen, L., J. P. Eastwood, J. P. Chittenden, and A. Masters (2016), Global
797 MHD simulations of Neptune’s magnetosphere, *Journal of Geophysical Research*
798 (*Space Physics*), 121(8), 7497–7513, doi:10.1002/2015JA022272.
- 799 Mejnertsen, L., J. P. Eastwood, H. Hietala, S. J. Schwartz, and J. P. Chittenden
800 (2018), Global MHD Simulations of the Earth’s Bow Shock Shape and Motion
801 Under Variable Solar Wind Conditions, *Journal of Geophysical Research (Space*
802 *Physics*), 123(1), 259–271, doi:10.1002/2017JA024690.
- 803 Mukai, T., S. Machida, Y. Saito, M. Hirahara, T. Terasawa, N. Kaya, T. Obara,
804 M. Ejiri, and A. Nishida (1994), The Low Energy Particle (LEP) Experiment on-
805 board the GEOTAIL Satellite., *Journal of Geomagnetism and Geoelectricity*, 46,
806 669–692, doi:10.5636/jgg.46.669.
- 807 Peredo, M., J. A. Slavin, E. Mazur, and S. A. Curtis (1995), Three-dimensional po-
808 sition and shape of the bow shock and their variation with Alfvénic, sonic and
809 magnetosonic Mach numbers and interplanetary magnetic field orientation, *Jour-*
810 *nal of Geophysical Research*, 100, 7907–7916, doi:10.1029/94JA02545.
- 811 Poedts, S., A. Kochanov, A. Lani, C. Scolini, C. Verbeke, S. Hosteaux, E. Chané,
812 H. Deconinck, N. Mihalache, F. Diet, D. Heynderickx, J. De Keyser, E. De
813 Donder, N. B. Crosby, M. Echim, L. Rodriguez, R. Vansintjan, F. Verstringe,
814 B. Mampaey, R. Horne, S. Glauert, P. Jiggens, R. Keil, A. Glover, G. Deprez, and
815 J.-P. Luntama (2020), The Virtual Space Weather Modelling Centre, *Journal of*
816 *Space Weather and Space Climate*, 10, 14, doi:10.1051/swsc/2020012.
- 817 Powell, K. G., P. L. Roe, T. J. Linde, T. I. Gombosi, and D. L. De Zeeuw (1999), A
818 Solution-Adaptive Upwind Scheme for Ideal Magnetohydrodynamics, *Journal of*
819 *Computational Physics*, 154, 284–309, doi:10.1006/jcph.1999.6299.
- 820 Raeder, J., D. Larson, W. Li, E. L. Kepko, and T. Fuller-Rowell (2008), OpenG-
821 GCM Simulations for the THEMIS Mission, *Space Science Reviews*, 141, 535–555,

- 822 doi:10.1007/s11214-008-9421-5.
- 823 Reigber, C., H. Lühr, and P. Schwintzer (2002), CHAMP mission status, *Advances*
824 *in Space Research*, 30, 129–134, doi:10.1016/S0273-1177(02)00276-4.
- 825 Reme, H., J. M. Bosqued, J. A. Sauvaud, A. Cros, J. Dandouras, C. Aoustin,
826 J. Bouyssou, T. Camus, J. Cuvilo, C. Martz, J. L. Medale, H. Perrier, D. Rome-
827 fort, J. Rouzaud, C. D'Uston, E. Möbius, K. Crocker, M. Granoff, L. M. Kistler,
828 M. Popecki, D. Hovestadt, B. Klecker, G. Paschmann, M. Scholer, C. W. Carl-
829 son, D. W. Curtis, R. P. Lin, J. P. McFadden, V. Formisano, E. Amata, M. B.
830 Bavassano-Cattaneo, P. Baldetti, G. Belluci, R. Bruno, G. Chionchio, A. di Lel-
831 lis, E. G. Shelley, A. G. Ghielmetti, W. Lennartsson, A. Korth, H. Rosenbauer,
832 R. Lundin, S. Olsen, G. K. Parks, M. McCarthy, and H. Balsiger (1997), The
833 Cluster Ion Spectrometry (CIS) Experiment, *Space Science Reviews*, 79, 303–350,
834 doi:10.1023/A:1004929816409.
- 835 Rème, H., C. Aoustin, J. M. Bosqued, I. Dandouras, B. Lavraud, J. A. Sauvaud,
836 A. Barthe, J. Bouyssou, T. Camus, O. Coeur-Joly, A. Cros, J. Cuvilo, F. Ducay,
837 Y. Garbarowitz, J. L. Medale, E. Penou, H. Perrier, D. Romefort, J. Rouzaud,
838 C. Vallat, D. Alcaydé, C. Jacquey, C. Mazelle, C. D'Uston, E. Möbius, L. M.
839 Kistler, K. Crocker, M. Granoff, C. Mouikis, M. Popecki, M. Vosbury, B. Klecker,
840 D. Hovestadt, H. Kucharek, E. Kuenneth, G. Paschmann, M. Scholer, N. Sckopke,
841 E. Seidenschwang, C. W. Carlson, D. W. Curtis, C. Ingraham, R. P. Lin, J. P.
842 McFadden, G. K. Parks, T. Phan, V. Formisano, E. Amata, M. B. Bavassano-
843 Cattaneo, P. Baldetti, R. Bruno, G. Chionchio, A. di Lellis, M. F. Marcucci,
844 G. Pallocchia, A. Korth, P. W. Daly, B. Graeve, H. Rosenbauer, V. Vasyliunas,
845 M. McCarthy, M. Wilber, L. Eliasson, R. Lundin, S. Olsen, E. G. Shelley, S. Fuse-
846 lier, A. G. Ghielmetti, W. Lennartsson, C. P. Escoubet, H. Balsiger, R. Friedel, J.-
847 B. Cao, R. A. Kovrashkin, I. Papamastorakis, R. Pellat, J. Scudder, and B. Son-
848 nerup (2001), First multispacecraft ion measurements in and near the Earth's
849 magnetosphere with the identical Cluster ion spectrometry (CIS) experiment,
850 *Annales Geophysicae*, 19, 1303–1354, doi:10.5194/angeo-19-1303-2001.
- 851 Ritter, P., H. Lühr, A. Viljanen, O. Amm, A. Pulkkinen, and I. Sillanpää (2004),
852 Ionospheric currents estimated simultaneously from CHAMP satellite and IMAGE
853 ground-based magnetic field measurements: a statistical study at auroral latitudes,
854 *Annales Geophysicae*, 22, 417–430, doi:10.5194/angeo-22-417-2004.

- 855 Rostoker, G. (1972), Geomagnetic indices., *Reviews of Geophysics and Space*
856 *Physics*, *10*, 935–950, doi:10.1029/RG010i004p00935.
- 857 Siscoe, G. L., G. M. Erickson, B. U. Sonnerup, N. C. Maynard, J. A. Schoendorf,
858 K. D. Siebert, D. R. Weimer, W. W. White, and G. R. Wilson (2001), The Mag-
859 netospheric Fluopause, in *AGU Spring Meeting Abstracts*, vol. 2001, pp. SM52D–
860 02.
- 861 Sofko, G. J., R. Greenwald, and W. Bristow (1995), Direct determination of large-
862 scale magnetospheric field-aligned currents with SuperDARN, *Geophysical Re-*
863 *search Letters*, *22*, 2041–2044, doi:10.1029/95GL01317.
- 864 Thomsen, M. F. (2004), Why K_p is such a good measure of magnetospheric convec-
865 tion, *Space Weather*, *2*, S11004, doi:10.1029/2004SW000089.
- 866 Tóth, G., I. V. Sokolov, T. I. Gombosi, D. R. Chesney, C. R. Clauer, D. L. de
867 Zeeuw, K. C. Hansen, K. J. Kane, W. B. Manchester, R. C. Oehmke, K. G. Pow-
868 ell, A. J. Ridley, I. I. Roussev, Q. F. Stout, O. Volberg, R. A. Wolf, S. Sazykin,
869 A. Chan, B. Yu, and J. Kóta (2005), Space Weather Modeling Framework: A
870 new tool for the space science community, *Journal of Geophysical Research (Space*
871 *Physics)*, *110*, A12226, doi:10.1029/2005JA011126.
- 872 Tóth, G., B. van der Holst, I. V. Sokolov, D. L. De Zeeuw, T. I. Gombosi, F. Fang,
873 W. B. Manchester, X. Meng, D. Najib, K. G. Powell, Q. F. Stout, A. Glo-
874 cer, Y.-J. Ma, and M. Opher (2012), Adaptive numerical algorithms in space
875 weather modeling, *Journal of Computational Physics*, *231*, 870–903, doi:
876 10.1016/j.jcp.2011.02.006.
- 877 Trotignon, J. G., P. M. E. Décréau, J. L. Rauch, X. Vallières, A. Rochel,
878 S. Kougblénou, G. Lointier, G. Facskó, P. Canu, F. Darrouzet, and A. Masson
879 (2010), The WHISPER Relaxation Sounder and the CLUSTER Active Archive,
880 *Astrophysics and Space Science Proceedings*, *11*, 185–208, doi:10.1007/978-90-481-
881 3499-1_12.
- 882 Trotignon, J.-G., Vallières, and the WHISPER team (2011), Calibration report of
883 the whisper measurements in the cluster active archive (caa), *Tech. rep.*, LPC2E
884 CNRS, caa-est-cr-whi.
- 885 Tsyganenko, N. A. (1995), Modeling the Earth's magnetospheric magnetic field
886 confined within a realistic magnetopause, *Journal of Geophysical Research*, *100*,
887 5599–5612, doi:10.1029/94JA03193.

- Vörös, Z., G. Facskó, M. Khodachenko, I. Honkonen, P. Janhunen, and M. Palmroth (2014), Windsock memory COnditioned RAM (CO-RAM) pressure effect: Forced reconnection in the Earth's magnetotail, *Journal of Geophysical Research (Space Physics)*, 119, 6273–6293, doi:10.1002/2014JA019857.
- Wang, Z.-D., and R. L. Xu (1994), Signatures of the magnetotail neutral sheet, *Geophysical Research Letters*, 21(19), 2087–2090, doi:10.1029/94GL01960.
- Weimer, D. R. (2005), Improved ionospheric electrodynamic models and application to calculating Joule heating rates, *Journal of Geophysical Research (Space Physics)*, 110, A05306, doi:10.1029/2004JA010884.
- Wiltberger, M., E. J. Rigler, V. Merkin, and J. G. Lyon (2017), Structure of High Latitude Currents in Magnetosphere-Ionosphere Models, *Space Science Reviews*, 206, 575–598, doi:10.1007/s11214-016-0271-2.
- Zhang, B., W. Lotko, M. J. Wiltberger, O. J. Brambles, and P. A. Damiano (2011), A statistical study of magnetosphere-ionosphere coupling in the Lyon-Fedder-Mobarry global MHD model, *Journal of Atmospheric and Solar-Terrestrial Physics*, 73, 686–702, doi:10.1016/j.jastp.2010.09.027.
- Zhang, B., K. A. Sorathia, J. G. Lyon, V. G. Merkin, J. S. Garretson, and M. Wiltberger (2019), GAMERA: A Three-dimensional Finite-volume MHD Solver for Non-orthogonal Curvilinear Geometries, *The Astrophysical Journal Supplement Series*, 244(1), 20, doi:10.3847/1538-4365/ab3a4c.

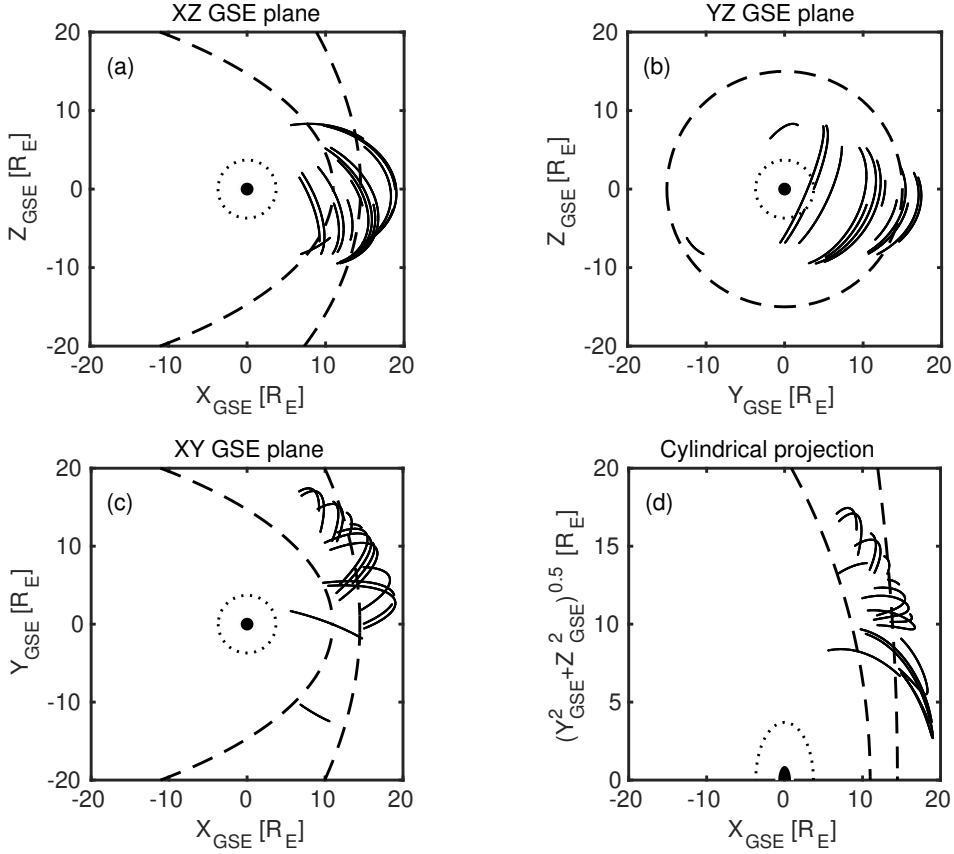


Figure 1. Cluster SC3 orbit in the solar wind in GSE system for all intervals (see Table 1).
 (a) XZ (b) YZ (c) XY (d) Cylindrical projection. Average bow-shock and magnetopause positions are drawn on all plots using dashed lines [Perego *et al.*, 1995; Tsyganenko, 1995, respectively]. The black dots at $3.7 R_E$ show the boundary of the GUMICS-4 inner magnetospheric domain. The black circle in the origo of all plots shows the size of the Earth.

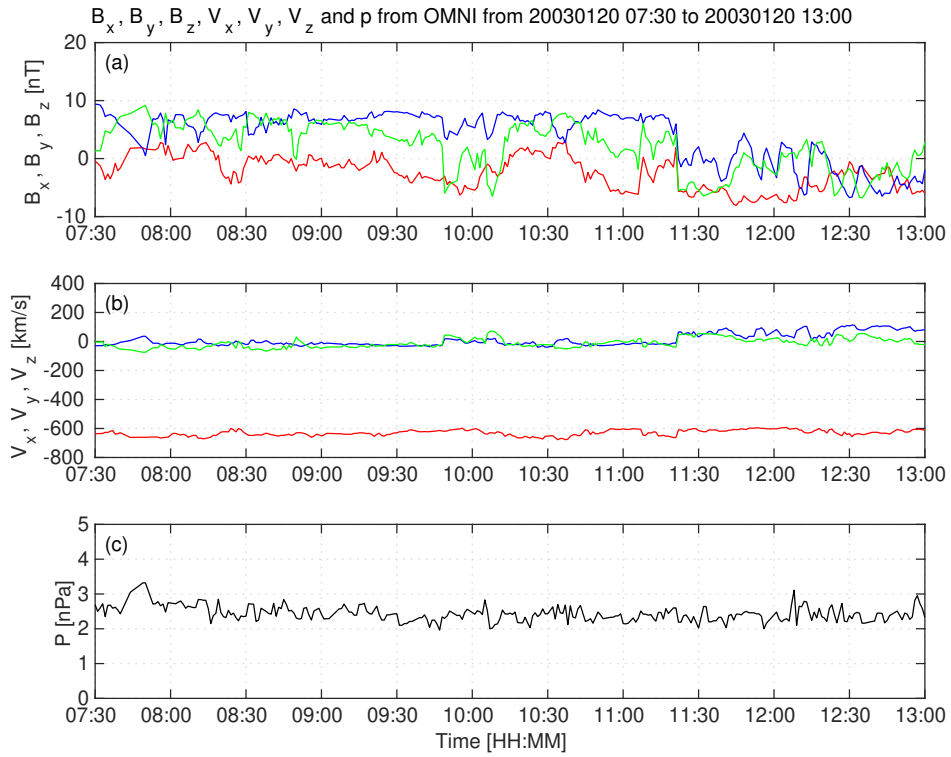
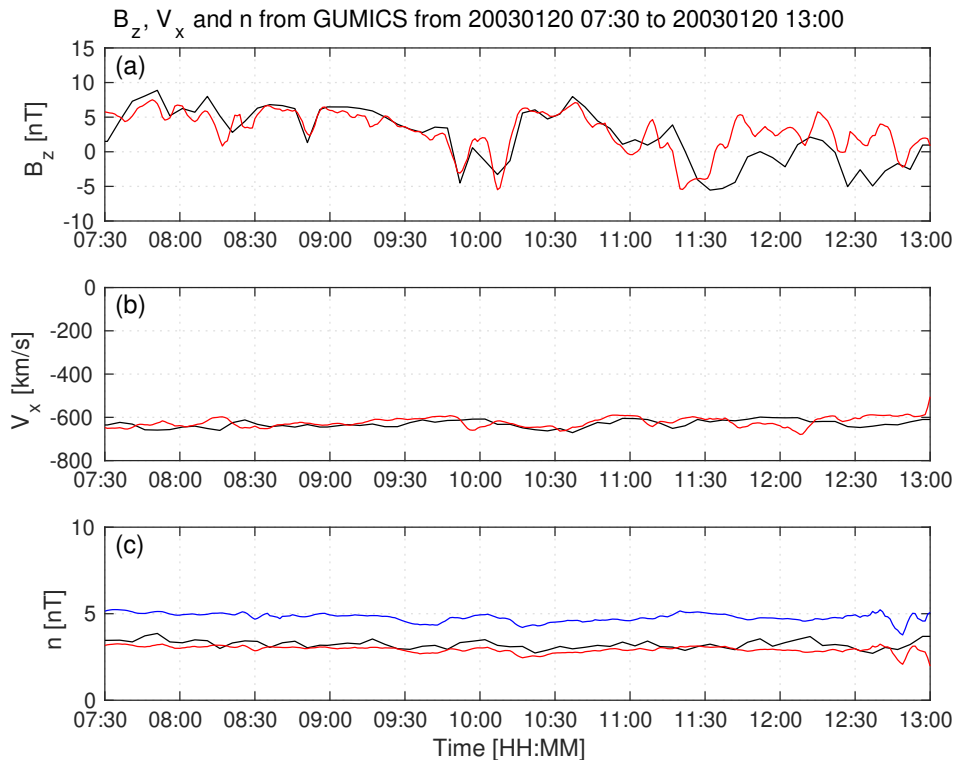
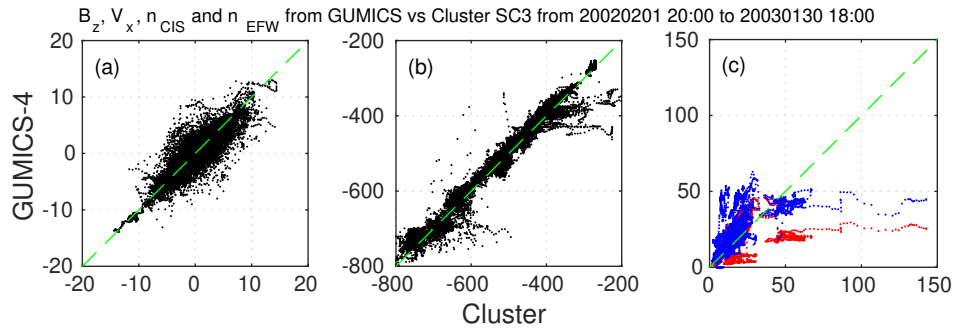


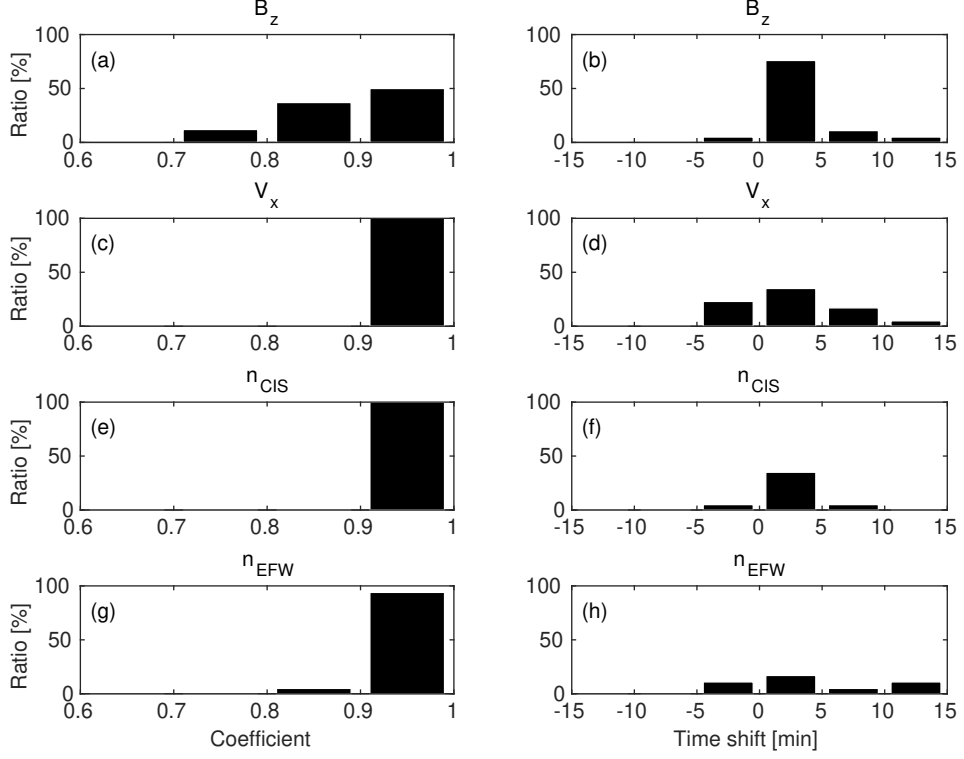
Figure 2. OMNI solar wind data in GSE system from 7:30 to 13:00 (UT) on January 20, 2003. (a) Magnetic field B_x (red), B_y (green) and B_z (blue) components. (b) Solar wind velocity V_x (red), V_y (green) and V_z (blue) components. (c) The P pressure of the solar wind (black).



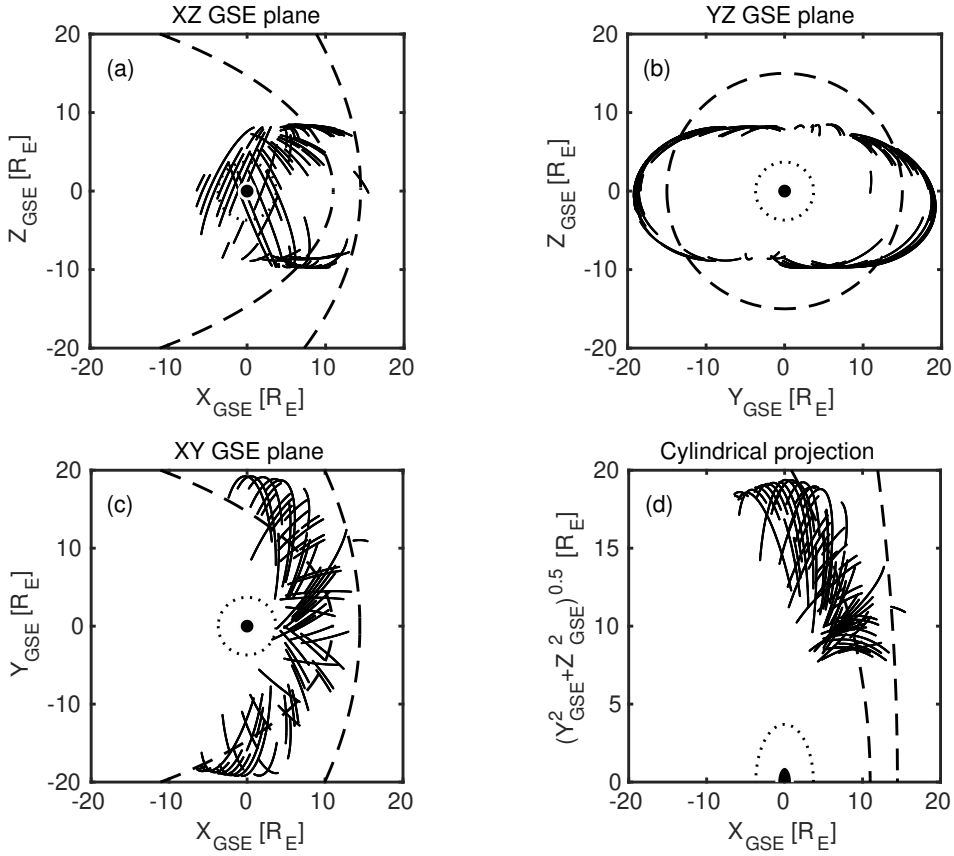
916 **Figure 3.** GUMICS-4 simulation results (black) and Cluster SC3 magnetic field Z component,
917 ion plasma moments (red) and electron density calculated from spacecraft potential (blue) from
918 January 20, 2003 from 7:30 to 13:00 (UT) in the solar wind in GSE system. (a) Magnetic field Z
919 component. (b) Solar wind velocity X component (c) Solar wind density.



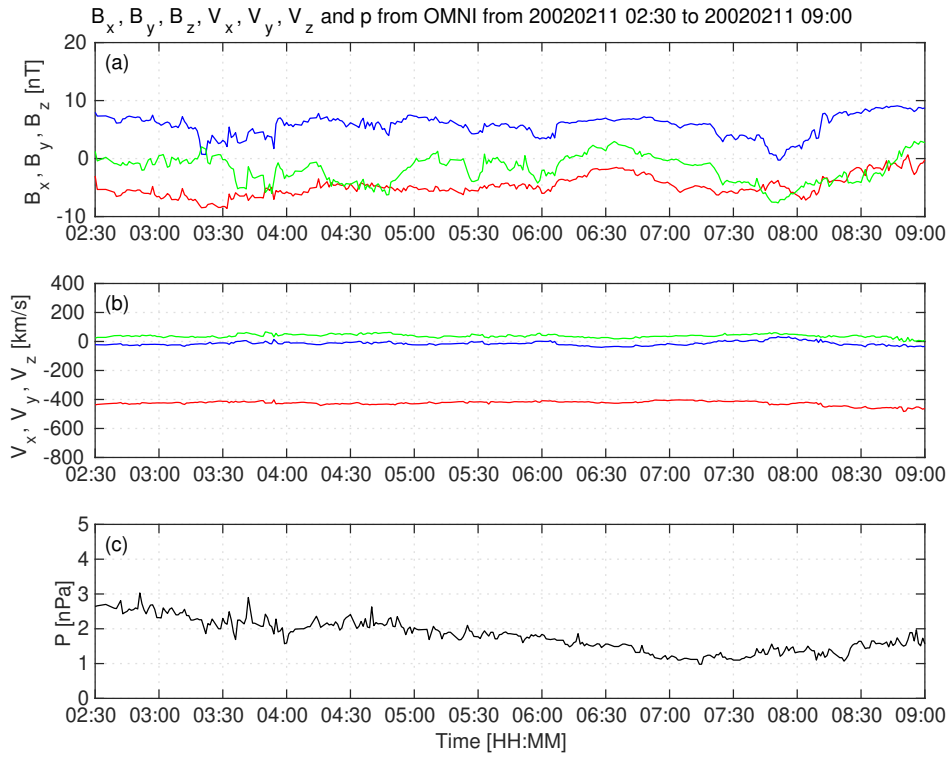
920 **Figure 4.** Scattered plots of the Cluster SC3 and GUMICS-4 simulations for all intervals in
921 the solar wind. The dashed line is the $y=x$ line. (a) Magnetic field Z component in GSE system.
922 (b) Solar wind velocity X component in GSE system. (c) Solar wind density measured by the
923 CIS HIA instrument (red) and calculated from the spacecraft potential (blue).



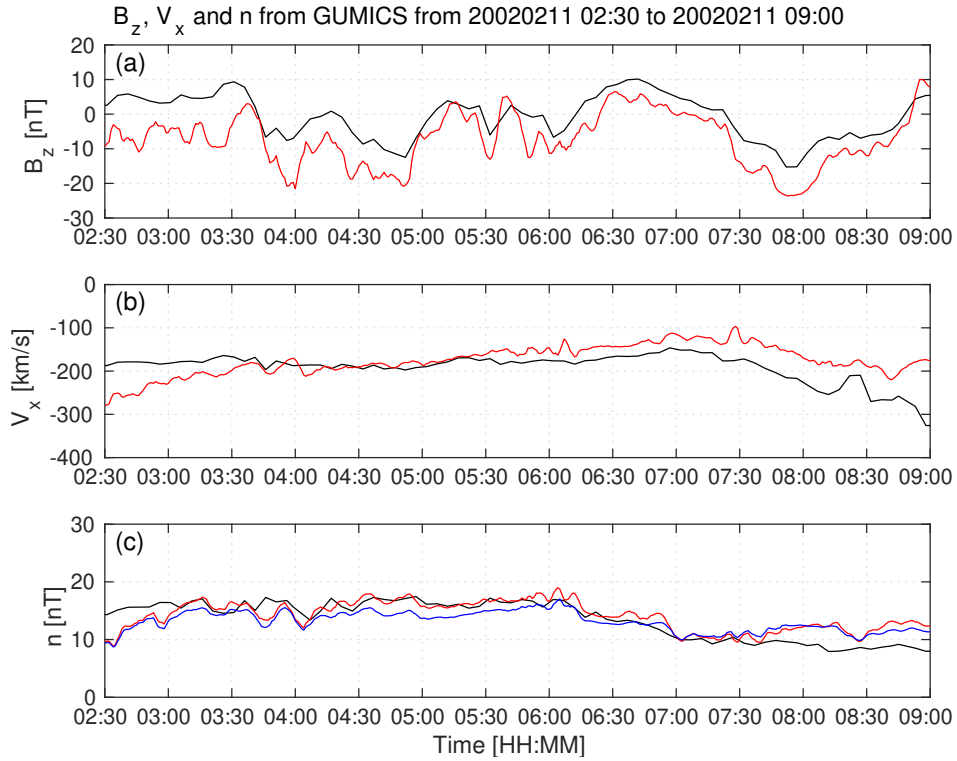
924 **Figure 5.** The distributions of the highest cross-correlation coefficients (a, c, e, g) of the
 925 magnetic field Z component (B_z) in GSE system, solar wind velocity X component (V_x) in GSE
 926 system, the solar wind density measured by the CIS HIA (n_{CIS}) instrument and calculated from
 927 the spacecraft potential (n_{EFW}), respectively, for all intervals in the solar wind. The distribu-
 928 tions of the corresponding time shifts (b, d, f, h) of the B_z , the V_x , the n_{CIS} and the n_{EFW}),
 929 respectively, for all intervals in the solar wind.



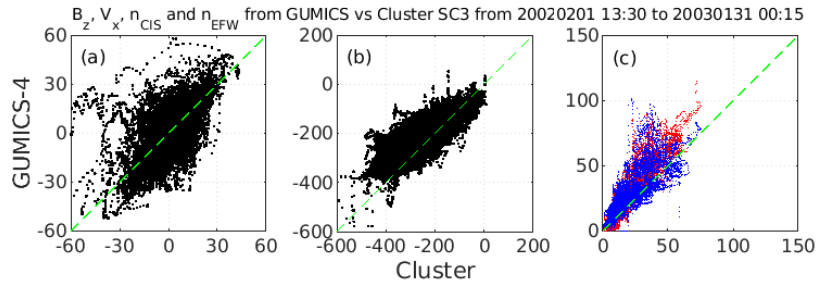
930 **Figure 6.** Cluster SC3 orbit in the magnetosheath in GSE system for all intervals (see Ta-
 931 ble 2). (a) XZ (b) YZ (c) XY (d) Cylindrical projection. Average bow-shock and magnetopause
 932 positions are drawn on all plots using dashed lines [Perez et al., 1995; Tsyganenko, 1995, respec-
 933 tively]. The black dots at $3.7 R_E$ show the boundary of the GUMICS-4 inner magnetospheric
 934 domain. The black circle in the origo of all plots shows the size of the Earth.



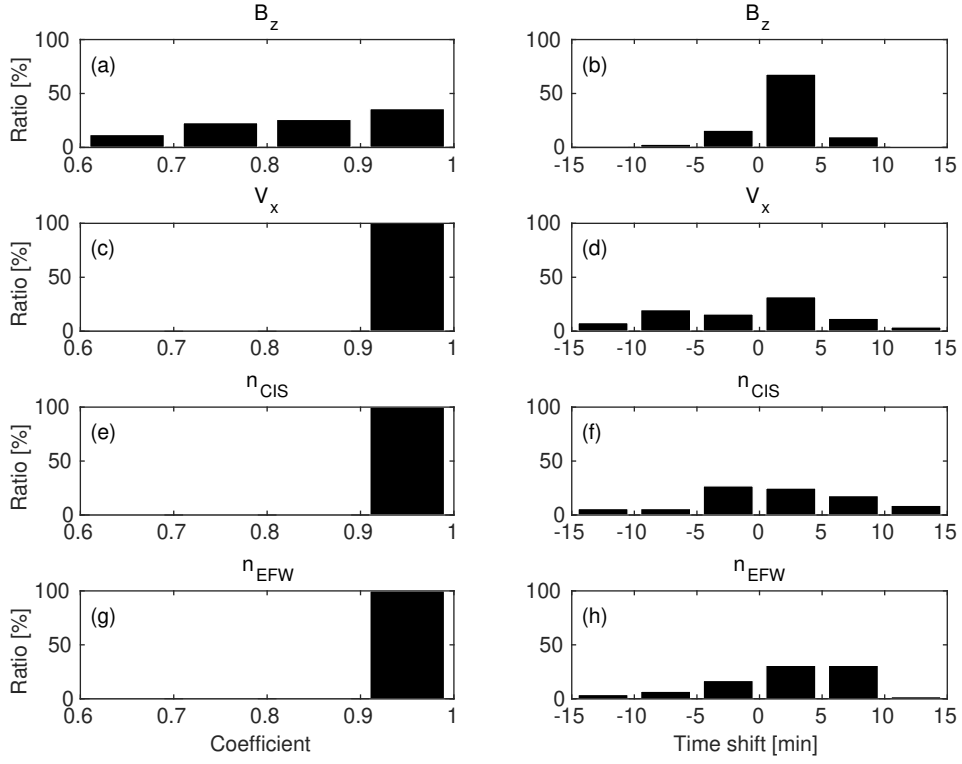
935 **Figure 7.** OMNI solar wind data in GSE system from 2:30 to 09:00 (UT) on February 11,
936 2002. (a) Magnetic field B_x (red), B_y (green) and B_z (blue) components. (b) Solar wind velocity
937 V_x (red), V_y (green) and V_z (blue) components. (c) The P pressure of the solar wind (black).



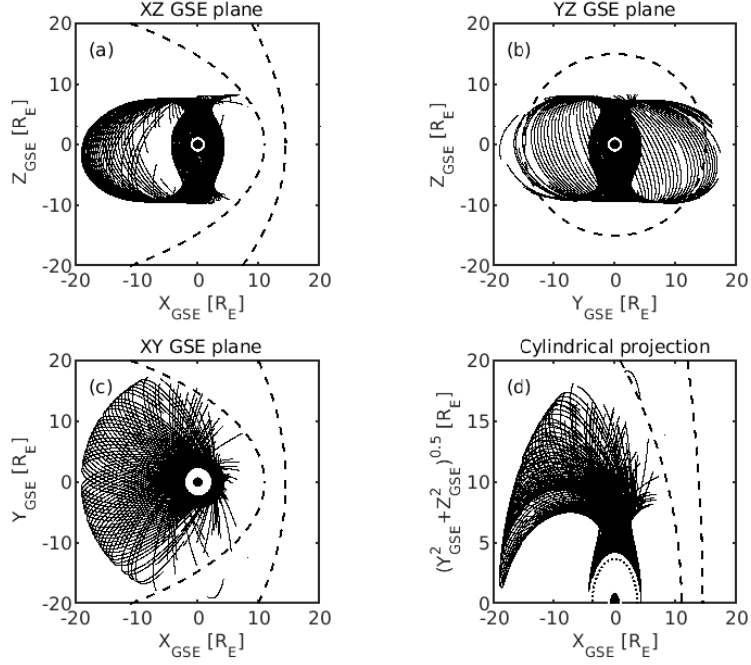
938 **Figure 8.** GUMICS-4 simulation results (black) and Cluster SC3 magnetic field Z component,
 939 ion plasma moments (red) and electron density calculated from spacecraft potential (blue) from
 940 February 11, 2002 from 2:30 to 9:00 (UT) in the magnetosheath in GSE system (a) Magnetic
 941 field Z component. (b) Solar wind velocity X component (c) Solar wind density.



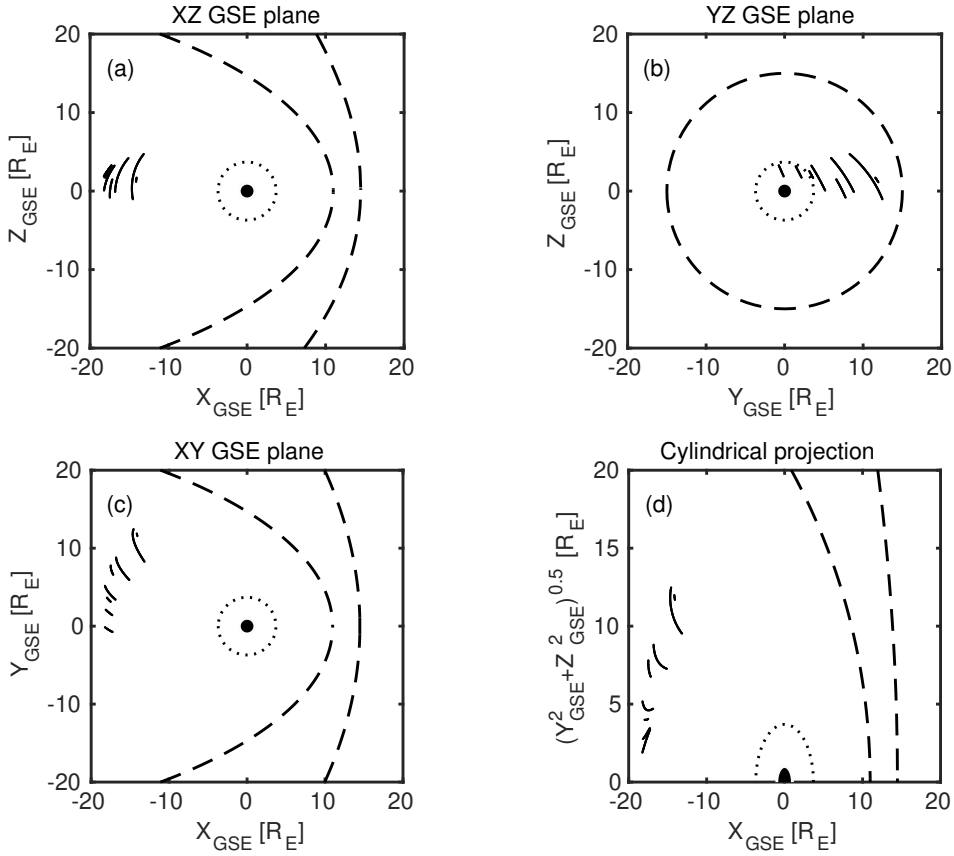
942 **Figure 9.** Scattered plots of the Cluster SC3 and GUMICS-4 simulations for all intervals in
 943 the magnetosheath in GSE system. The dashed line is the $y=x$ line. (a) Magnetic field Z com-
 944 ponent. (b) Solar wind velocity X component. (c) Solar wind density measured by the CIS HIA
 945 instrument (red) and calculated from the spacecraft potential (blue).



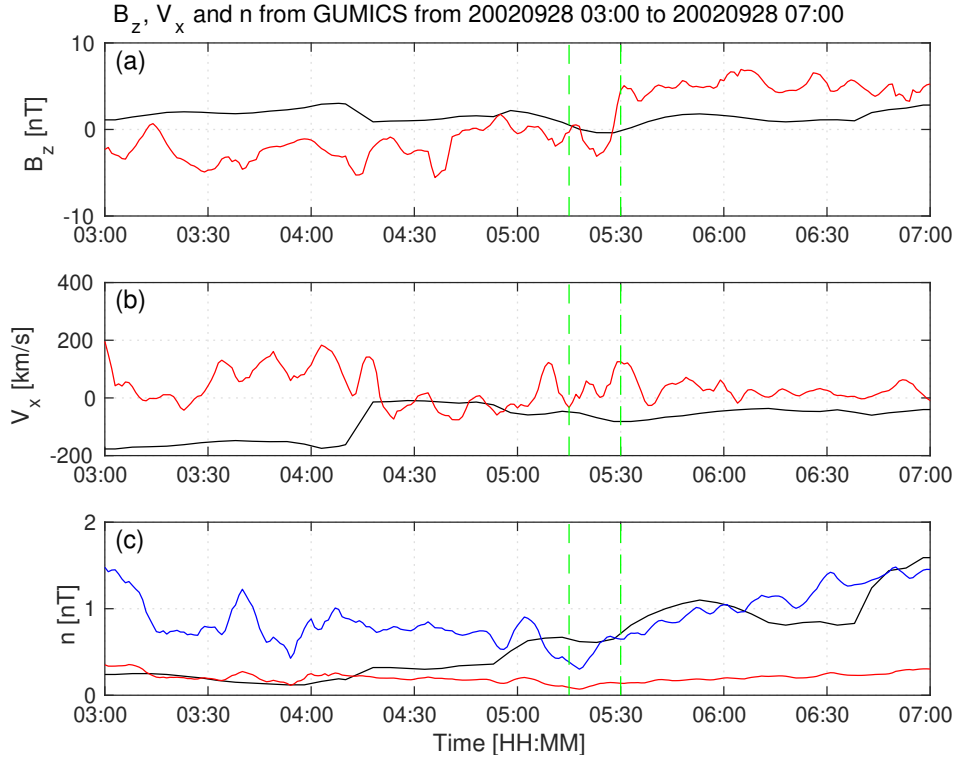
946 **Figure 10.** The distributions of the cross-correlation coefficients (a, c, e, g) of the magnetic
947 field Z component (B_z) in GSE system, solar wind velocity X component (V_x) in GSE system,
948 the solar wind density measured by the CIS HIA (n_{CIS}) instrument and calculated from the
949 spacecraft potential (n_{EFW}), respectively, for all intervals in the magnetosheath. The distribu-
950 tions of the time shifts (b, d, f, h) of the B_z , the V_x , the n_{CIS} and the n_{EFW} , respectively, for
951 all intervals in the magnetosheath.



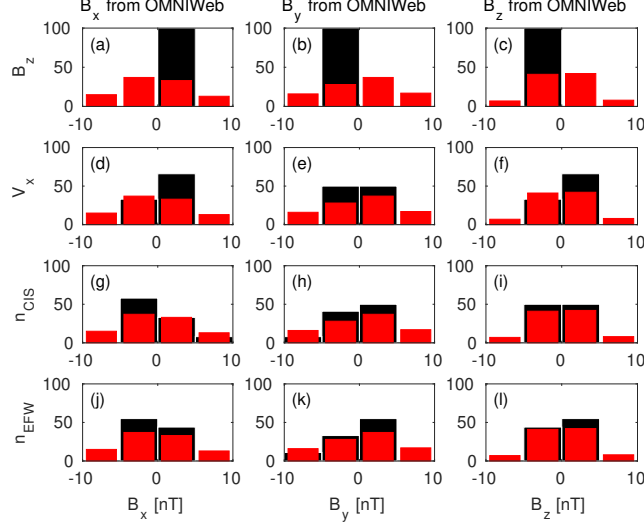
952 **Figure 11.** Cluster SC3 orbit in the magnetosphere in GSE system for all intervals (see Ta-
953 ble 3). (a) XZ (b) YZ (c) XY (d) Cylindrical projection. Average bow-shock and magnetopause
954 positions are drawn on all plots using dashed lines [Perego *et al.*, 1995; Tsyganenko, 1995, respec-
955 tively]. The black dots at $3.7 R_E$ show the boundary of the GUMICS-4 inner magnetospheric
956 domain. The black circle in the origo of all plots shows the size of the Earth.



957 **Figure 12.** Cluster SC3 orbit in the tail in GSE system for all intervals (see Table 6). (a) XZ
 958 (b) YZ (c) XY (d) Cylindrical projection. Average bow-shock and magnetopause positions are
 959 drawn on all plots using dashed lines [Peredo *et al.*, 1995; Tsyganenko, 1995, respectively]. The
 960 black dots at $3.7 R_E$ show the boundary of the GUMICS–4 inner magnetospheric domain. The
 961 black circle in the origo of all plots shows the size of the Earth.



962 **Figure 13.** GUMICS-4 simulation results (black) and Cluster SC3 magnetic field Z compo-
 963 nent, ion plasma moments (red) and electron density calculated from spacecraft potential (blue)
 964 from September 28, 2002 from 3:00 to 7:00 (UT) in the tail in GSE system. (a) Magnetic field
 965 Z component. (b) Solar wind velocity X component (c) Solar wind density. From 05:15 to 05:30
 966 between the green dashed vertical lines both the Cluster SC3 and the virtual spaceprobe of the
 967 GUMICS-4 simulation cross the neutral sheet multiple times.



968 **Figure 14.** The black distributions of the B_x , the B_y and the B_z OMNI solar wind magnetic
 969 field components when the agreement of the Cluster SC3 measurements and the GUMICS-4
 970 simulations are poor in the solar wind (see Table 7). The B_z , the V_x , the n_{CIS} and the n_{EFW}
 971 are the magnetic field GSE Z component, the plasma ion velocity X GSE component, the solar
 972 wind density measured by the CIS HIA instrument and the calculated from the EFW spacecraft
 973 potential, respectively. (a, b, c) Distribution of OMNI B_x , B_y , B_z when the agreement of B_z
 974 is poor. (d, e, f) Distribution of OMNI B_x , B_y , B_z when the agreement of V_x is poor. (g, h, i)
 975 Distribution of OMNI B_x , B_y , B_z when the agreement of n_{CIS} is poor. (j, k, l) Distribution of
 976 OMNI B_x , B_y , B_z when the agreement of n_{EFW} is poor. The values are in percentage unitss in
 977 the distributions. The red distributions of (a, d, g, j), (b, e, h, k) and (c, f, i, l) are the distribu-
 978 tion of the B_x , the B_y , and the B_z components of the OMNI solar wind magnetic field during the
 979 1-year run from January 29, 2002, to February 2, 2003, in GSE reference frame, respectively.

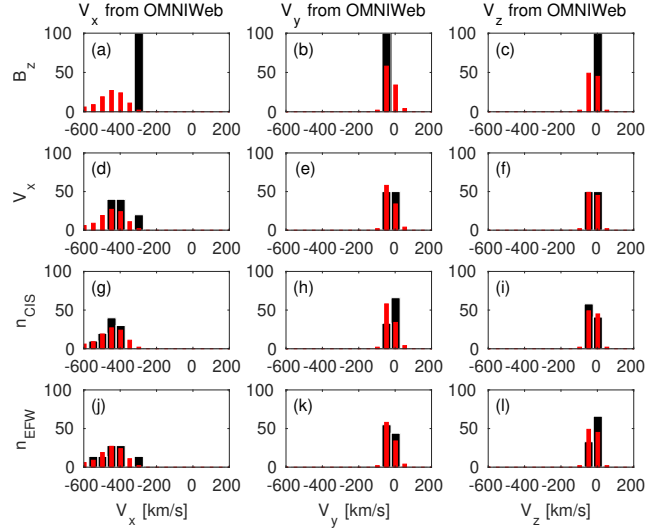
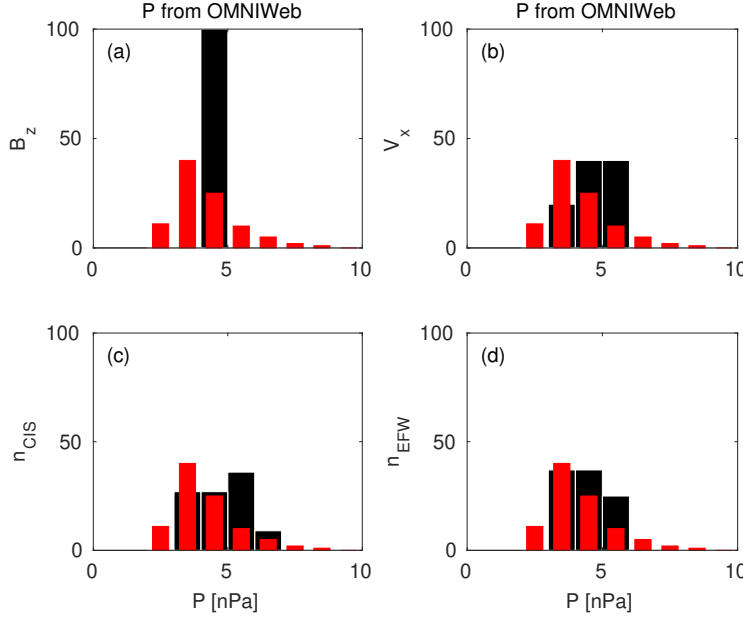
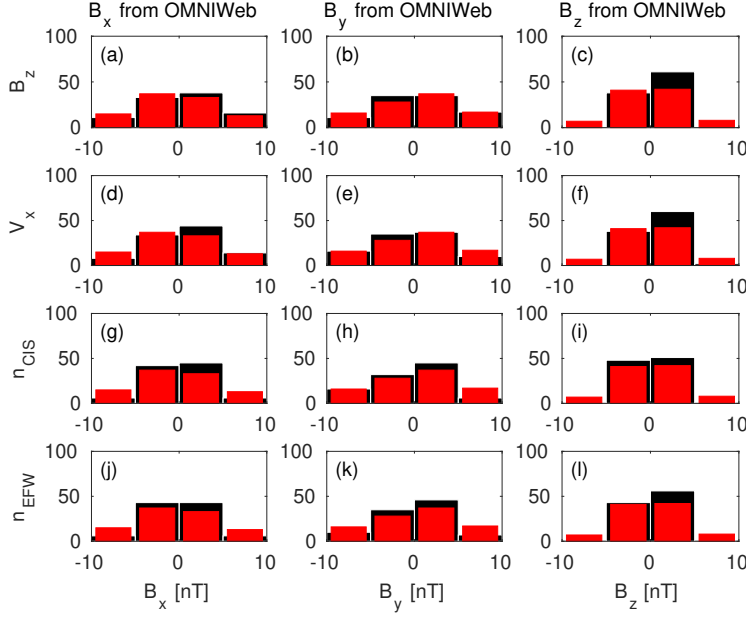


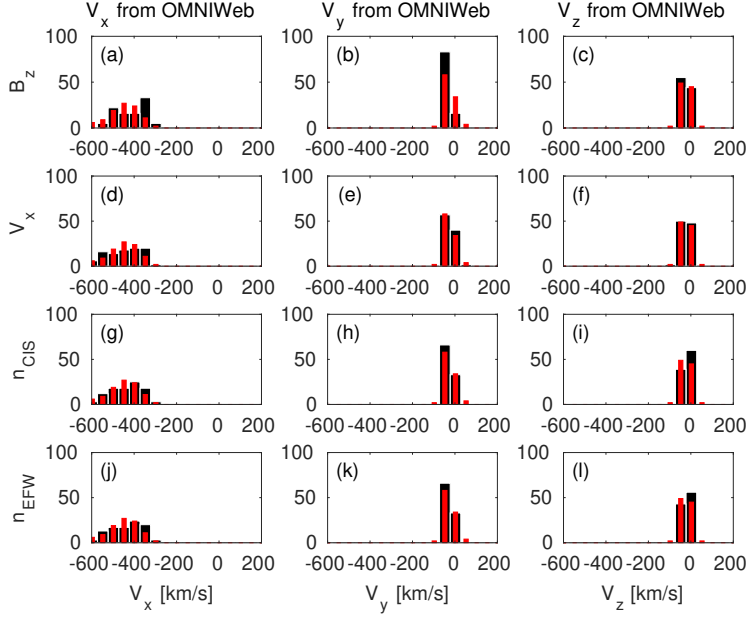
Figure 15. The black distributions of the V_x , the V_y and the V_z OMNI solar wind velocity components when the agreement of the Cluster SC3 measurements and the GUMICS-4 simulations are poor in the solar wind (see Table 7). The B_z , the V_x , the n_{CIS} and the n_{EFW} are the magnetic field GSE Z component, the plasma ion velocity X GSE component, the solar wind density measured by the CIS HIA instrument and the calculated from the EFW spacecraft potential, respectively. (a, b, c) Distribution of OMNI V_x , V_y , V_z when the agreement of B_z is poor. (d, e, f) Distribution of OMNI V_x , V_y , V_z when the agreement of V_x is poor. (g, h, i) Distribution of OMNI V_x , V_y , V_z when the agreement of n_{CIS} is poor. (j, k, l) Distribution of OMNI V_x , V_y , V_z when the agreement of n_{EFW} is poor. The values are in percentage units in the distributions. The red distributions of (a, d, g, j), (b, e, h, k) and (c, f, i, l) are the distributions of the V_x , the V_y and the V_z components of the OMNI solar wind velocity during the 1-year run from January 29, 2002 to February 2, 2003 in GSE reference frame, respectively.



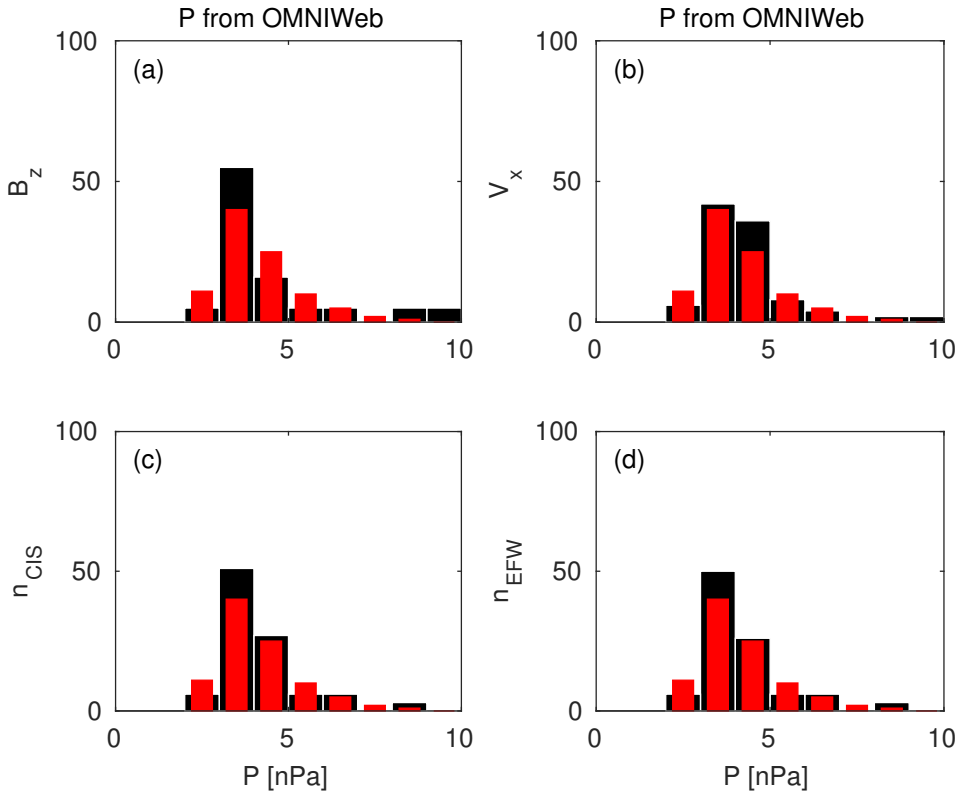
992 **Figure 16.** The black distributions of the P solar wind dynamic pressure calculated from
993 OMNI parameters when the agreement of the Cluster SC3 measurements and the GUMICS–4
994 simulations are poor in the solar wind (see Table 7). The B_z , V_x , n_{CIS} and n_{EFW} are the mag-
995 netic field GSE Z component, the velocity X GSE component, the solar wind density measured
996 by the CIS HIA instrument and calculated from the EFW spacecraft potential, respectively.
997 (a, b, c, d) The distribution of the P calculated from OMNI data when the agreement of the B_z ,
998 the V_x , the n_{CIS} or the n_{EFW} are poor. The values are in percentage units in the distributions.
999 The red distributions of (a, b, c, d) are the distributions of the P solar wind dynamic pressure
1000 calculated from the OMNI solar wind parameters during the 1-year run from January 29, 2002,
1001 to February 2, 2003, in GSE reference frame.



1002 **Figure 17.** The black distributions of the B_x , the B_y and the B_z OMNI solar wind magnetic
 1003 field components when the agreement of the Cluster SC3 measurements and the GUMICS-4
 1004 simulations are poor in the magnetosheath (see Table 8). The B_z , the V_x , the n_{CIS} and the
 1005 n_{EFW} are the magnetic field GSE Z component, the plasma ion velocity X GSE component,
 1006 the solar wind density measured by the CIS HIA instrument and the calculated from the EFW
 1007 spacecraft potential, respectively. (a, b, c) Distribution of OMNI B_x , B_y , B_z when the agree-
 1008 ment of B_z is poor. (d, e, f) Distribution of OMNI B_x , B_y , B_z when the agreement of V_x is
 1009 poor. (g, h, i) Distribution of OMNI B_x , B_y , B_z when the agreement of n_{CIS} is poor. (j, k, l)
 1010 Distribution of OMNI B_x , B_y , B_z when the agreement of n_{EFW} is poor. The values are in per-
 1011 centage units in the distributions. The red distributions of (a, d, g, j), (b, e, h, k) and (c, f, i, l)
 1012 are the distribution of the B_x , the B_y , and the B_z components of the OMNI solar wind magnetic
 1013 field during the 1-year run from January 29, 2002, to February 2, 2003, in GSE reference frame,
 1014 respectively.



1015 **Figure 18.** The black distributions of the V_x , the V_y and the V_z OMNI solar wind velocity
 1016 components when the agreement of the Cluster SC3 measurements and the GUMICS–4 simula-
 1017 tions are poor in the magnetosheath (see Table 8). The B_z , the V_x , the n_{CIS} and the n_{EFW} are
 1018 the magnetic field GSE Z component, the plasma ion velocity X GSE component, the solar wind
 1019 density measured by the CIS HIA instrument and the calculated from the EFW spacecraft po-
 1020 tential, respectively. (a, b, c) Distribution of OMNI V_x , V_y , V_z when the agreement of B_z is poor.
 1021 (d, e, f) Distribution of OMNI V_x , V_y , V_z when the agreement of V_x is poor. (g, h, i) Distribution
 1022 of OMNI V_x , V_y , V_z when the agreement of n_{CIS} is poor. (j, k, l) Distribution of OMNI V_x , V_y ,
 1023 V_z when the agreement of n_{EFW} is poor. The values are in percentage units in the distributions.
 1024 The red distributions of (a, d, g, j), (b, e, h, k) and (c, f, i, l) are the distributions of the V_x , the
 1025 V_y and the V_z components of the OMNI solar wind velocity during the 1-year run from January
 1026 29, 2002 to February 2, 2003 in GSE reference frame, respectively.



1027 **Figure 19.** The black distributions of the P solar wind dynamic pressure calculated from
 1028 OMNI parameters when the agreement of the Cluster SC3 measurements and the GUMICS–4
 1029 simulations are poor in the magnetosheath (see Table 8). The B_z , V_x , n_{CIS} and n_{EFW} are
 1030 the magnetic field GSE Z component, the velocity X GSE component, the solar wind density
 1031 measured by the CIS HIA instrument and calculated from the EFW spacecraft potential, respec-
 1032 tively. (a, b, c, d) The distribution of the P calculated from OMNI data when the agreement of
 1033 the B_z , the V_x , the n_{CIS} or the n_{EFW} are poor. The values are in percentage units in the dis-
 1034 tributions. The red distributions of (a, b, c, d) are the distributions of the P solar wind dynamic
 1035 pressure calculated from the OMNI solar wind parameters during the 1-year run from January
 1036 29, 2002 to February 2, 2003 in GSE reference frame.

Start/End	C_{B_z}	δt_{B_z}	C_{V_x}	δt_{V_x}	$C_{n_{CIS}}$	$\delta t_{n_{CIS}}$	$C_{n_{EFW}}$	$\delta t_{n_{EFW}}$
	[min]		[min]		[min]		[min]	
20020201 20:00/0203 04:00	0.97	3	1.00	12	0.96	3	0.98	3
20020211 13:00/0212 12:00	0.86	2	1.00	0	0.99	19	0.99	18
20020218 09:00/0219 02:00	0.95	1	1.00	-4	1.00	-3	0.97	-2
20020219 06:30/0219 15:00	0.96	1	0.99	-1	0.99	-60	1.00	60
20020220 18:30/0222 00:00	0.90	4	1.00	4	0.93	-20	0.98	3
20020318 17:30/0319 02:30	0.91	2	1.00	21	0.98	51	0.99	6
20020412 20:30/0413 02:00	0.91	5	0.99	-53	0.94	60	0.98	12
20021227 12:00/1228 03:00	0.84	4	1.00	-2	0.99	-21	0.99	22
20021229 20:00/1230 16:00	0.76	1	1.00	1	0.99	-30	0.98	43
20030106 06:00/0106 19:00	0.82	5	1.00	7	0.99	3	0.95	-60
20030108 07:00/0109 03:30	0.56	10	1.00	41	0.99	9	0.97	-56
20030113 08:30/0113 18:00	0.94	3	1.00	5	1.00	3	0.97	-1
20030120 07:30/0120 13:00	0.86	3	1.00	8	1.00	4	1.00	-55
20030122 12:00/0123 14:00	0.85	2	1.00	3	1.00	3	0.92	-60
20030124 18:00/0126 00:00	0.78	3	1.00	0	0.99	-60	0.99	60
20030127 16:00/0128 06:00	0.89	-1	1.00	-3	0.96	1	0.89	12
20030129 12:00/0130 18:00	0.92	2	1.00	4	0.95	-59	0.98	1

Table 1. The studied solar wind intervals. The correlation coefficients (C_{B_z} , C_{V_x} , $C_{n_{CIS}}$, $C_{n_{EFW}}$) and time shift (δt_{V_x} , $\delta t_{n_{CIS}}$, $\delta t_{n_{EFW}}$) in minutes of the magnetic field GSE Z component (B_z), solar wind velocity X component (V_x), CIS and EFW densities (n_{CIS} , n_{EFW}).

Table 2: The studied magnetosheath intervals. The correlation coefficients (C_{B_z} , C_{V_x} , $C_{n_{CIS}}$, $C_{n_{EFW}}$) and time shift (δt_{V_x} , $\delta t_{n_{CIS}}$, $\delta t_{n_{EFW}}$) in minutes of the magnetic field GSE Z component (B_z), solar wind velocity X component (V_x), CIS and EFW densities (n_{CIS} , n_{EFW}). In the empty slots the correlation calculation gives invalid result.

Start/End	C_{B_z}	δt_{B_z}	C_{V_x}	δt_{V_x}	$C_{n_{CIS}}$	$\delta t_{n_{CIS}}$	$C_{n_{EFW}}$	$\delta t_{n_{EFW}}$
		[min]		[min]		[min]		[min]
20020201 13:30/0201 18:30	0.92	1	0.98	57	0.99	60	0.98	60
20020208 18:15/0209 00:00	0.78	3	0.95	60	0.98	-53	0.98	-54
20020211 02:30/0211 09:00	0.81	0	0.99	-21	1.00	0	0.99	0
20020212 16:30/0212 21:00	0.86	3	1.00	54	0.99	30	0.99	30
20020219 17:30/0219 23:00	0.78	4	0.99	37	1.00	6	1.00	6
20020222 23:00/0223 06:30	0.69	1	0.97	-60	0.99	-52	0.99	-48
20020227 16:30/0227 23:15	0.53	60	0.98	-31	1.00	-38	1.00	-11
20020310 18:30/0311 00:30	0.98	3	0.98	20	0.99	8	0.99	-2
20020311 14:00/0311 19:00	0.88	5	0.97	36	0.99	-3	0.99	-40
20020406 19:00/0407 01:15	0.79	1	0.97	-60	0.98	-56	0.98	-56
20020410 17:30/0410 23:00	0.89	5	0.99	-52	1.00	3	1.00	5
20020411 11:30/0411 16:30	0.84	3	0.99	40	0.99	3	0.99	3
20020418 18:30/0418 22:45	0.93	59	0.99	-60	0.99	60	0.98	60
20020421 04:30/0421 07:45	0.98	55	1.00	-60	1.00	-60	1.00	-60
20020422 11:45/0422 15:45	0.77	-5	0.98	-17	0.99	-15	0.99	-16
20020423 08:30/0423 12:30	0.94	31	1.00	4	0.99	16	1.00	16
20020430 12:30/0430 17:00	0.81	58	0.99	23	0.99	-18		
20020505 07:00/0505 11:15	0.83	59	0.99	32	0.99	-60		
20020506 19:15/0507 00:15	0.89	-28	0.99	-60	0.98	-36		
20020507 17:30/0507 23:00	0.94	1	0.99	47	0.99	-47		
20020514 22:45/0515 03:00	0.82	49	0.99	-60	0.99	32	0.99	-37
20020517 07:00/0517 12:15	0.76	-6	1.00	-5	0.99	-4	0.99	-3
20020518 13:30/0518 19:30	0.76	1	0.99	11	0.98	-2	0.98	-2

Continued on next page

Table 2 – *Continued from previous page*

Start/End	C_{B_z}	δt_{B_z}	C_{V_x}	δt_{V_x}	$C_{n_{CIS}}$	$\delta t_{n_{CIS}}$	$C_{n_{EFW}}$	$\delta t_{n_{EFW}}$
		[min]		[min]		[min]		[min]
20020519 20:00/0520 03:30	0.98	2	1.00	-9	0.99	-4	0.99	-50
20020520 10:45/0520 20:15	0.80	1	0.99	-3	0.95	-1	0.99	-1
20020522 02:00/0522 08:45	0.53	52	0.99	4	0.99	11	0.99	22
20020527 02:15/0527 17:15	0.80	-3	0.99	-2	0.98	0	0.99	0
20020530 05:00/0530 10:30	0.30	3	1.00	-23	0.99	4	0.99	3
20020601 19:30/0602 01:00	0.68	-2	1.00	17	0.99	-6	0.99	-7
20020602 21:45/0603 17:45	0.65	-5	0.99	0	0.98	3	0.99	3
20020605 10:30/0606 06:00	0.20	0	0.99	-7	0.98	10	0.98	9
20020607 18:00/0607 22:00	0.93	-35	1.00	-34	0.99	16	0.99	15
20020608 01:15/0608 18:15	0.54	-4	1.00	-39	0.97	-6	0.97	-6
20020610 01:30/0610 09:30	0.80	5	1.00	8	0.99	3	1.00	-7
20020610 11:00/0611 01:00	0.89	-4	1.00	-35	0.99	24	0.99	7
20020612 18:30/0613 06:15	0.45	-2	0.99	-7	0.97	-3	0.97	-33
20020615 07:00/0615 23:30			1.00	47	0.98	-3	0.98	-5
20020617 05:00/0618 03:45	0.79	3	1.00	28	0.98	9	0.99	8
20020620 04:00/0620 11:00	0.65	-8	0.99	-6	0.98	11	0.98	6
20020622 14:30/0622 18:00	0.99	56	1.00	33	1.00	16	1.00	16
20021201 04:15/1202 07:45	0.41	1	1.00	2	0.99	6	0.99	6
20021203 15:30/1204 19:30	0.72	1	0.99	60	0.98	59	0.98	59
20021207 00:30/1207 07:45	0.53	38	0.99	-50	0.99	-20	0.99	20
20021208 09:30/1209 08:00	0.72	3	0.99	-36	0.98	5	0.98	5
20021212 23:30/1213 14:30	0.53	5	1.00	36	0.99	-3	0.95	-56
20021213 21:15/1214 09:30	0.96	5	1.00	-35	0.99	-5	0.99	-46
20021215 12:45/1216 18:00	0.80	2	0.99	-60	0.95	-60	0.98	30
20021217 16:30/1218 01:45	0.91	2	1.00	-54	0.99	3	0.99	3
20021220 01:30/1220 06:15	0.93	0	1.00	60	0.99	2	0.99	3
20021223 02:15/1223 13:00	0.93	1	0.97	39	0.94	50	0.99	-14
20021223 14:00/1223 22:30	0.88	1	1.00	-2	0.99	-1	1.00	-3
20021224 19:00/1225 01:45	0.96	0	1.00	-43	0.99	12	0.99	28

Continued on next page

Table 2 – *Continued from previous page*

Start/End	C_{B_z}	δt_{B_z}	C_{V_x}	δt_{V_x}	$C_{n_{CIS}}$	$\delta t_{n_{CIS}}$	$C_{n_{EFW}}$	$\delta t_{n_{EFW}}$
		[min]		[min]		[min]		[min]
20021225 23:45/1226 07:15	0.97	7	1.00	-18	0.99	56	0.99	56
20021226 23:00/1227 09:45	0.83	2	1.00	2	0.99	4	0.99	2
20021229 11:45/1229 17:00	0.63	2	1.00	-32	0.99	49	0.99	48
20021230 17:45/1231 01:00	0.74	1	0.99	55	0.98	60	0.98	22
20021231 23:00/0101 05:15	0.92	2	1.00	0	0.99	-54	1.00	-56
20030105 14:00/0105 21:00	0.73	1	1.00	1	1.00	-60	0.99	-60
20030106 23:15/0107 03:00	0.70	4	0.99	41	1.00	56	1.00	-60
20030109 08:45/0109 16:15			0.91	-55	0.98	-13	0.98	-25
20030110 07:15/0110 15:15	0.95	1	0.99	-7	0.99	2	0.98	11
20030111 08:15/0111 22:30	0.88	1	0.99	-59	0.94	-15	0.94	8
20030112 17:30/0113 00:15	0.98	0	1.00	-47	0.99	39	0.99	51
20030114 00:30/0114 08:30	0.86	-1	0.99	-60	0.98	23	0.98	8
20030116 10:15/0116 17:45	0.64	60	0.93	52	0.99	60	0.99	30
20030117 09:30/0117 13:30	0.70	-3	1.00	7	1.00	-31	1.00	-33
20030118 23:30/0119 03:45	0.97	3	1.00	-12	1.00	7	0.99	7
20030119 21:00/0120 01:00	0.96	3	1.00	6	1.00	38	1.00	20
20030121 06:30/0121 11:30	0.87	-3	0.98	40	0.99	8	1.00	8
20030122 04:45/0122 09:30	0.76	-2	1.00	1	1.00	-7	1.00	-4
20030126 01:45/0126 06:30	0.90	3	0.99	-15	1.00	-51	0.99	24
20030127 08:15/0127 13:00	1.00	10	1.00	-60	0.99	-1	0.99	1
20030128 12:30/0128 17:15	0.77	60	0.99	-22	0.99	-5	0.99	21
20030130 19:45/0131 00:15	0.98	2	0.99	52	0.99	8	0.99	8

Table 3: The studied magnetosphere intervals (UT).

Start/End
20020213 23:00/0214 01:30
20020217 18:30/0218 02:00
20020220 00:45/0220 12:00
20020222 11:15/0222 20:15
20020225 02:15/0225 08:30
20020227 06:00/0227 12:00
20020302 00:00/0302 03:15
20020306 10:00/0306 18:30
20020308 17:30/0309 06:00
20020311 02:15/0311 12:00
20020313 11:15/0314 00:15
20020316 04:45/0316 08:00
20020318 09:00/0318 14:45
20020320 20:30/0320 23:55
20020323 04:00/0323 09:45
20020327 23:45/0328 06:15
20020330 07:15/0330 12:45
20020401 19:30/0401 22:00
20020406 09:30/0406 18:00
20020408 15:00/0409 00:00
20020410 23:30/0411 09:45
20020413 08:30/0413 19:00
20020416 18:00/0417 04:30
20020418 06:00/0418 12:00
20020420 15:00/0420 23:00
20020422 20:00/0423 07:00
20020425 08:30/0425 18:00
20020430 04:40/0430 12:00
20020504 14:30/0504 16:45

Continued on next page

Table 3 – *Continued from previous page*

Start/End
20020505 02:30/0505 07:00
20020507 01:30/0507 15:45
20020508 11:00/0510 04:15
20020512 02:45/0512 09:30
20020514 10:30/0514 12:45
20020519 00:30/0519 19:30
20020521 01:30/0521 22:00
20020523 23:30/0524 02:00
20020524 19:00/0525 08:15
20020526 07:30/0526 10:30
20020528 20:00/0529 05:00
20020531 02:15/0531 13:30
20020602 04:30/0602 07:30
20020602 12:00/0602 21:30
20020604 08:30/0605 07:00
20020606 14:30/0607 16:30
20020609 06:00/0609 20:00
20020611 11:00/0612 13:00
20020614 01:00/0614 16:00
20020616 08:00/0616 18:00
20020620 13:30/0622 01:00
20020623 13:00/0623 17:00
20020624 04:00/0624 10:15
20020630 17:45/0701 15:00
20020701 21:00/0703 10:30
20020703 23:00/0706 03:15
20020707 01:00/0708 23:00
20020710 11:30/0714 03:30
20020714 15:45/0715 15:30
20020716 23:30/0717 16:00

Continued on next page

Table 3 – *Continued from previous page*

Start/End
20020718 05:45/0722 11:00
20020722 23:45/0728 01:00
20020728 02:00/0804 03:45
20020804 04:45/0811 06:15
20020811 07:30/0816 01:00
20020816 15:30/0818 09:00
20020818 10:00/0825 11:30
20020825 13:00/0901 14:15
20020901 17:15/0903 23:30
20020905 02:15/0906 16:30
20020907 10:30/0908 17:00
20020908 18:00/0915 19:30
20020915 21:00/0922 22:30
20020923 00:00/0923 23:30
20020924 03:30/0928 22:45
20020928 23:30/0930 01:00
20020930 02:15/1006 17:00
20021006 17:45/1007 03:30
20021007 05:00/1007 17:30
20021008 07:30/1010 22:00
20021010 22:30/1012 22:30
20021012 23:00/1014 06:30
20021014 09:00/1016 04:00
20021016 14:00/1019 00:15
20021019 01:30/1019 22:00
20021021 04:00/1022 19:30
20021022 22:30/1026 02:30
20021026 04:00/1029 20:15
20021030 01:30/1102 08:00
20021102 22:00/1104 22:00

Continued on next page

Table 3 – *Continued from previous page*

Start/End
20021106 00:00/1107 18:00
20021108 02:00/1109 18:45
20021111 00:00/1112 01:30
20021113 03:45/1114 14:15
20021115 20:30/1116 23:00
20021118 01:00/1118 23:30
20021120 17:00/1121 06:00
20021122 21:30/1124 01:00
20021125 04:00/1126 08:30
20021127 20:00/1128 18:30
20021130 04:00/1201 01:30
20021202 14:30/1203 09:00
20021204 22:00/1205 19:30
20021207 09:00/1207 16:30
20021207 18:00/1207 22:00
20021209 16:30/1210 14:30
20021212 13:45/1212 21:30
20021214 13:30/1214 20:00
20021214 21:00/1215 07:30
20021216 21:00/1217 15:00
20021219 08:00/1219 19:30
20021221 15:45/1221 23:15
20021222 00:30/1222 08:45
20021224 02:30/1224 14:00
20021226 10:00/1226 19:00
20021228 19:30/1229 02:30
20021229 04:00/1229 10:00
20021231 05:00/1231 18:45
20030102 12:30/0102 20:45
20030104 20:45/0105 06:00

Continued on next page

Table 3 – *Continued from previous page*

Start/End
20030105 07:00/0105 13:30
20030107 05:45/0107 21:00
20030109 17:00/0110 00:45
20030112 00:00/0112 09:15
20030112 10:30/0112 16:00
20030114 11:00/0114 20:00
20030116 20:30/0116 22:45
20030119 04:30/0119 09:30
20030119 14:00/0119 17:00
20030121 13:30/0121 21:30
20030126 07:30/0126 15:45
20030128 17:45/0129 08:15
20030131 01:30/0131 11:45

Table 4: Intervals around the studied bow shock crossings. The Cluster SC3 crossed the bow shock in all cases. The 2nd column shows whether the bow shock is visible in the GUMICS–4 simulations.

Start/End	GUMICS Bow Shock
20020201 12:00/0202 00:00	+
20020203 00:00/0203 12:00	+
20020206 06:00/0206 18:00	+
20020208 18:00/0209 06:00	+
20020211 06:00/0211 18:00	+
20020212 12:00/0212 18:00	+
20020213 12:00/0213 18:00	+
20020216 00:00/0216 12:00	+
20020217 06:00/0217 12:00	-
20020218 06:00/0218 18:00	+
20020219 00:00/0219 18:00	+
20020220 12:00/0221 00:00	+
20020221 18:00/0222 00:00	+
20020301 06:00/0301 12:00	+
20020304 12:00/0304 18:00	+
20020306 00:00/0306 06:00	+
20020307 00:00/0307 06:00	+
20020308 06:00/0308 12:00	+
20020309 06:00/0309 12:00	+
20020310 12:00/0311 00:00	+
20020311 18:00/0312 00:00	+
20020313 00:00/0313 06:00	-
20020314 00:00/0314 12:00	+
20020316 06:00/0316 18:00	+
20020318 12:00/0319 00:00	+
20020323 12:00/0323 18:00	+

Continued on next page

Table 4 – *Continued from previous page*

Start/End	GUMICS Bow Shock
20020325 18:00/0326 06:00	–
20020327 06:00/0327 12:00	+
20020329 18:00/0330 00:00	–
20020402 00:00/0402 06:00	+
20020405 18:00/0406 00:00	–
20020407 00:00/0407 06:00	–
20020409 06:00/0409 12:00	–
20020410 12:00/0410 18:00	–
20020411 12:00/0411 18:00	–
20020413 00:00/0413 06:00	+
20020413 18:00/0414 06:00	+
20020420 00:00/0420 06:00	+
20020423 12:00/0423 23:00	+
20020427 00:00/0427 06:00	+
20020428 06:00/0428 12:00	+
20020430 18:00/0501 00:00	+
20020505 06:00/0505 18:00	–
20020507 18:00/0509 06:00	+
20020510 06:00/0510 12:00	+
20020513 12:00/0513 18:00	+
20020515 00:00/0515 06:00	–
20020520 00:00/0520 06:00	+
20020522 06:00/0522 12:00	+
20020522 18:00/0523 06:00	+
20021206 06:00/1207 06:00	+
20021218 00:00/1219 00:00	+
20021220 18:00/1221 00:00	+
20021221 00:00/1221 12:00	+
20021222 12:00/1223 00:00	+
20021223 00:00/1223 06:00	+

Continued on next page

Table 4 – *Continued from previous page*

Start/End	GUMICS Bow Shock
20021225 06:00/1226 00:00	+
20021227 06:00/1228 00:00	+
20021228 00:00/1228 12:00	+
20021229 12:00/1230 00:00	+
20030101 06:00/0102 00:00	+
20030103 06:00/0103 12:00	+
20030104 00:00/0104 18:00	+
20030106 00:00/0107 00:00	+
20030108 00:00/0108 12:00	+
20030113 00:00/0114 06:00	+
20030115 00:00/0115 12:00	+
20030118 18:00/0119 00:00	+
20030120 00:00/0121 12:00	+
20030122 06:00/0122 12:00	+
20030123 12:00/0124 00:00	+
20030124 12:00/0124 18:00	+
20030126 00:00/0126 06:00	+
20030127 00:00/0127 18:00	+
20030128 06:00/0128 18:00	+
20030129 06:00/0129 12:00	+
20030130 18:00/0131 00:00	+

Table 5: Intervals around the studied magnetopause crossings.
The Cluster SC3 crossed the magnetopause in all cases. The
2nd column shows whether the magnetopause is visible in the
GUMICS–4 simulations.

Start/End	GUMICS Magnetopause
20020203 06:00/0203 12:00	+
20020206 06:00/0206 12:00	-
20020211 00:00/0211 06:00	+
20020218 00:00/0218 06:00	+
20020225 06:00/0225 12:00	+
20020302 00:00/0302 06:00	+
20020306 18:00/0307 00:00	-
20020308 12:00/0308 18:00	-
20020311 12:00/0311 18:00	+
20020313 18:00/0314 00:00	-
20020314 00:00/0314 06:00	+
20020323 06:00/0323 12:00	+
20020330 12:00/0330 18:00	-
20020404 06:00/0404 12:00	-
20020409 00:00/0409 06:00	-
20020418 12:00/0418 18:00	+
20020422 12:00/0422 18:00	-
20020429 18:00/0430 00:00	-
20020507 12:00/0507 18:00	-
20020509 06:00/0509 12:00	-
20020510 00:00/0510 06:00	-
20020514 18:00/0515 00:00	-
20020519 12:00/0519 18:00	-
20020520 12:00/0521 00:00	-
20020522 00:00/0522 06:00	-
20020529 00:00/0529 12:00	-

Continued on next page

Table 5 – *Continued from previous page*

Start/End	GUMICS Magnetopause
20020530 06:00/0530 18:00	–
20020531 18:00/0601 00:00	–
20020602 18:00/0603 00:00	–
20020604 06:00/0604 12:00	–
20020605 06:00/0606 18:00	–
20020607 12:00/0608 06:00	+
20020609 00:00/0609 06:00	–
20020610 00:00/0610 06:00	–
20020611 00:00/0611 12:00	–
20020612 06:00/0614 00:00	–
20020614 18:00/0615 06:00	–
20020616 00:00/0616 12:00	+
20020620 00:00/0620 18:00	–
20020622 06:00/0622 18:00	–
20020704 12:00/0705 00:00	–
20020706 00:00/0706 12:00	+
20020709 00:00/0709 18:00	–
20020715 18:00/0716 12:00	–
20030105 06:00/0105 18:00	+
20030110 00:00/0110 12:00	+
20030112 12:00/0112 18:00	–
20030117 06:00/0117 12:00	+
20030121 06:00/0121 12:00	+
20030122 00:00/0122 06:00	–
20030126 18:00/0127 00:00	+
20030128 12:00/0128 18:00	+
20030129 00:00/0129 12:00	+
20030131 12:00/0201 00:00	+

Start/End	GUMICS Neutral Sheet
20020901 19:00/0902 00:00	–
20020906 14:00/0906 16:30	+
20020913 17:30/0913 20:00	+
20020918 13:00/0918 14:30	–
20020920 20:30/0921 02:00	+
20020928 03:00/0928 07:00	+
20021002 16:00/1003 00:00	–
20021014 12:30/1014 23:00	+
20021017 03:00/1017 04:00	–

¹⁰⁴⁴ **Table 6.** Intervals around the studied neutral sheet crossings in the tail. The Cluster SC3
¹⁰⁴⁵ crossed the neutral sheet in all cases. The 2nd column shows whether the neutral sheet is visible
¹⁰⁴⁶ in the GUMICS–4 simulations.

Start/End	OMNI			Cluster SC3			
	B_z [nT]	V_x [km/s]	P [cm $^{-3}$]	B_z	V_x	n_{CIS}	n_{EFW}
20020201 20:00/0203 04:00	-1.25	-373.52	4.08	y	y	n	y
20020211 13:00/0212 12:00	0.03	-533.11	2.18	y	y	y	y
20020218 09:00/0219 02:00	2.56	-362.41	3.46	y	n	n	y
20020219 06:30/0219 15:00	3.55	-401.63	1.25	y	y	n	n
20020220 18:30/0222 00:00	1.95	-440.18	1.96	y	y	n	y
20020318 17:30/0319 02:30	3.79	-429.30	15.34	y	n	n	n
20020412 20:30/0413 02:00	-1.81	-420.35	3.24	y	n	n	y
20021227 12:00/1228 03:00	0.09	-714.40	2.72	y	n	n	y
20021229 20:00/1230 16:00	-0.37	-526.40	2.26	y	y	n	n
20030106 06:00/0106 19:00	2.25	-399.91	1.50	y	n	n	n
20030108 07:00/0109 03:30	-0.58	-280.80	2.97	n	n	y	n
20030113 08:30/0113 18:00	0.68	-397.83	1.72	y	y	y	n
20030120 07:30/0120 13:00	2.16	-630.69	2.43	y	y	y	y
20030122 12:00/0123 14:00	0.13	-608.96	3.41	y	y	y	n
20030124 18:00/0126 00:00	-0.71	-739.68	2.87	y	y	n	n
20030127 16:00/0128 06:00	-0.92	-451.84	3.12	y	y	n	n
20030129 12:00/0130 18:00	-3.09	-450.00	3.96	y	y	n	y

1047 **Table 7.** The average OMNI input parameters in the solar wind and the good/bad agreement
 1048 of the GUMICS–4 simulations to the Cluster B_z magnetic field component, the V_x solar wind
 1049 speed component, the n_{CIS} solar wind density measured by the Cluster CIS HIA instrument and
 1050 the n_{EFW} solar wind density calculated from the spacecraft potential measured by the Cluster
 1051 EFW instrument in the solar wind.

Table 8: The average OMNI input parameters in the solar wind and the good/bad agreement of the GUMICS–4 simulations to the Cluster B_z magnetic field component, the V_x solar wind speed component, the n_{CIS} solar wind density measured by the Cluster CIS HIA instrument and the n_{EFW} solar wind density calculated from the spacecraft potential measured by the Cluster EFW instrument in the magnetosheath.

Start/End	OMNI			Cluster SC3			
	B_z	V_x	P	B_z	V_x	n_{CIS}	n_{EFW}
	[nT]	[km/s]	[cm $^{-3}$]				
20020201 13:30/0201 18:30	0.19	-342.87	4.62	y	n	n	n
20020208 18:15/0209 00:00	-0.48	-508.16	1.61	y	n	n	n
20020211 02:30/0211 09:00	-1.85	-425.67	1.78	y	y	y	y
20020212 16:30/0212 21:00	2.98	-509.22	2.34	y	n	n	n
20020219 17:30/0219 23:00	1.46	-431.50	1.46	y	y	y	y
20020222 23:00/0223 06:30	0.86	-391.22	1.14	y	n	n	n
20020227 16:30/0227 23:15	1.89	-343.13	1.52	n	n	n	n
20020310 18:30/0311 00:30	-2.81	-379.46	1.78	y	y	y	y
20020311 14:00/0311 19:00	1.63	-371.43	2.68	n	n	n	n
20020406 19:00/0407 01:15	-2.71	-333.13	0.93	y	n	n	n
20020410 17:30/0410 23:00	0.31	-312.43	4.42	n	n	y	y
20020411 11:30/0411 16:30	-1.50	-494.02	4.25	y	y	n	n
20020418 18:30/0418 22:45	-0.92	-450.82	0.30	n	n	n	n
20020421 04:30/0421 07:45	0.40	-455.69	1.37	n	n	n	n
20020422 11:45/0422 15:45	0.25	-419.98	1.14	n	n	y	y
20020423 08:30/0423 12:30	2.77	-507.99	6.82	n	n	n	n
20020430 12:30/0430 17:00	2.15	-479.51	3.02	n	n	n	n
20020505 07:00/0505 11:15	0.20	-336.81	1.74	n	n	n	n
20020506 19:15/0507 00:15	0.78	-390.00	2.46	y	n	n	n
20020507 17:30/0507 23:00	2.87	-392.40	3.49	y	n	n	n
20020514 22:45/0515 03:00	-2.42	-414.01	1.82	n	n	n	n

Continued on next page

Table 8 – *Continued from previous page*

Start/End	OMNI			Cluster SC3			
	B_z [nT]	V_x [km/s]	P $[cm^{-3}]$	B_z	V_x	n_{CIS}	n_{EFW}
20020517 07:00/0517 12:15	-0.39	-379.32	1.52	y	y	y	y
20020518 13:30/0518 19:30	0.63	-345.87	1.59	n	n	y	y
20020519 20:00/0520 03:30	4.75	-408.56	1.12	y	y	y	y
20020520 10:45/0520 20:15	0.74	-448.89	1.93	y	y	y	y
20020522 02:00/0522 08:45	-1.07	-398.12	1.63	n	y	y	y
20020527 02:15/0527 17:15	-3.11	-542.53	2.07	y	y	y	y
20020530 05:00/0530 10:30	0.03	-493.86	2.08	y	n	y	y
20020601 19:30/0602 01:00	-3.38	-342.27	4.16	y	y	y	y
20020602 21:45/0603 17:45	0.38	-435.47	1.89	y	y	y	y
20020605 10:30/0606 06:00	-0.42	-394.49	1.08	y	y	n	n
20020607 18:00/0607 22:00	-1.60	-291.85	1.80	y	y	y	y
20020608 01:15/0608 18:15	0.06	-335.39	2.74	y	n	y	y
20020610 01:30/0610 09:30	1.60	-465.52	3.00	y	y	y	y
20020610 11:00/0611 01:00	-2.27	-419.86	2.16	y	n	y	y
20020612 18:30/0613 06:15	-1.13	-351.03	1.16	y	y	y	y
20020615 07:00/0615 23:30	-1.16	-334.27	2.84	n	n	y	y
20020617 05:00/0618 03:45	0.78	-351.47	1.87	y	n	y	y
20020620 04:00/0620 11:00	0.46	-485.48	1.73	y	y	y	y
20020622 14:30/0622 18:00	-0.72	-429.02	1.93	n	n	y	y
20021201 04:15/1202 07:45	-1.09	-499.23	2.62	y	y	y	y
20021203 15:30/1204 19:30	0.34	-449.09	2.06	y	n	n	n
20021207 00:30/1207 07:45	0.80	-451.80	7.33	n	n	y	y
20021208 09:30/1209 08:00	0.60	-600.27	1.49	y	n	y	y
20021212 23:30/1213 14:30	0.10	-337.77	1.32	y	n	n	n
20021213 21:15/1214 09:30	-0.74	-361.19	2.99	y	n	y	y
20021215 12:45/1216 18:00	1.32	-479.48	1.53	y	n	n	n
20021217 16:30/1218 01:45	4.56	-393.99	2.49	y	n	y	y
20021220 01:30/1220 06:15	-1.21	-530.62	3.01	y	n	y	y

Continued on next page

Table 8 – *Continued from previous page*

Start/End	OMNI			Cluster SC3			
	B_z [nT]	V_x [km/s]	P $[cm^{-3}]$	B_z	V_x	n_{CIS}	n_{EFW}
20021223 02:15/1223 13:00	-2.32	-516.12	2.22	y	n	n	n
20021223 14:00/1223 22:30	0.89	-519.77	2.55	y	y	y	y
20021224 19:00/1225 01:45	0.88	-523.86	3.41	y	n	y	y
20021225 23:45/1226 07:15	-0.61	-414.38	2.21	y	y	n	n
20021226 23:00/1227 09:45	-1.79	-618.14	6.20	y	y	y	y
20021229 11:45/1229 17:00	-0.41	-580.12	2.39	y	n	n	n
20021230 17:45/1231 01:00	-1.01	-483.60	1.93	y	n	n	y
20021231 23:00/0101 05:15	0.60	-418.95	1.94	y	n	n	n
20030105 14:00/0105 21:00	-0.03	-414.46	1.69	y	n	n	n
20030106 23:15/0107 03:00	-1.62	-392.29	1.56	n	n	n	n
20030109 08:45/0109 16:15	1.45	-272.82	2.31	n	n	n	n
20030110 07:15/0110 15:15	-2.11	-401.03	2.72	y	n	y	y
20030111 08:15/0111 22:30	-0.20	-433.33	1.24	y	n	n	y
20030112 17:30/0113 00:15	1.53	-389.62	1.45	y	n	n	n
20030114 00:30/0114 08:30	-1.67	-388.53	2.27	y	n	n	y
20030116 10:15/0116 17:45	-1.20	-328.91	1.22	n	n	n	n
20030117 09:30/0117 13:30	-1.36	-327.09	2.55	y	y	y	y
20030118 23:30/0119 03:45	6.41	-459.46	4.82	y	y	y	y
20030119 21:00/0120 01:00	1.52	-597.95	2.38	y	n	y	y
20030121 06:30/0121 11:30	-1.77	-670.25	1.50	y	n	n	n
20030122 04:45/0122 09:30	0.11	-588.87	2.30	y	n	y	y
20030126 01:45/0126 06:30	-0.24	-713.82	2.75	y	y	y	y
20030127 08:15/0127 13:00	7.94	-509.30	0.47	y	n	y	y
20030128 12:30/0128 17:15	4.95	-443.83	4.15	y	y	y	y
20030130 19:45/0131 00:15	4.21	-510.33	2.63	y	n	y	y